

PAPER • OPEN ACCESS

Uncertainty and worst-case expectation analysis for multiphysics QPR simulations

To cite this article: Piotr Putek et al 2025 Supercond. Sci. Technol. 38 025002

View the <u>article online</u> for updates and enhancements.

You may also like

- Physico chemical and phase separation characterization of high molecular PLLA blended with low molecular PCL obtained from solvent cast processes
 Daniela Arbeiter, Thomas Eickner, Stefan Oschatz et al.
- The software defined implantable modular platform (STELLA) for preclinical deep brain stimulation research in rodents Franz Plocksties, Maria Kober, Christoph Niemann et al.
- Towards an optimised deep brain stimulation using a large-scale computational network and realistic volume conductor model Konstantinos Spiliotis, Konstantin Butenko, Jens Starke et al.

Supercond. Sci. Technol. 38 (2025) 025002 (19pp)

https://doi.org/10.1088/1361-6668/ad9a0d

Uncertainty and worst-case expectation analysis for multiphysics QPR simulations

Piotr Putek^{1,*}, Simon B Adrian¹, Marc Wenskat^{2,3} and Ursula van Rienen^{1,4}

E-mail: piotr.putek@uni-rostock.de

Received 5 April 2024, revised 20 October 2024 Accepted for publication 20 November 2024 Published 6 January 2025



Abstract

Quadrupole resonators (QPRs) serve to characterize superconducting samples. Like any cavity, during operation, they will deviate from the design geometry for various reasons. Those deviations can be static, stemming from manufacturing variations reflected in the manufacturing tolerances, or dynamic, such as electromagnetic radiation pressure (Lorentz detuning) or microphonics. As a result, a QPR's measurement accuracy and general operation can be severely limited. In particular, during operation, it became evident that the third operating mode of typical QPRs is mainly affected. In this work, by solving the underlying multiphysics problem with random input parameters, we predict the predominant sources of significant measurement bias in surface resistance. On the one hand, we employ the stochastic collocation method compound with the polynomial chaos expansion (PC-SCM) to quantify uncertainties in the physical model governed by a coupled electro-stress-heat problem. On the other hand, we explore the perturbation analysis to calculate the mean-worst-scenario bound of the merit functions due to the first-order truncation of the Taylor expansion around mean parameter values. The developed method allows us to study the effect of a small nonlinear deformation on the performance of the QPR. Finally, we discuss the simulation results and their implication for the operational conditions of the QPRs.

Keywords: uncertainty quantification, shape perturbation analysis, Lorentz force (LF) detuning, weakly coupled E-S-H problem, quadrupole resonator

© <u>•</u>

Original Content from this work may be used under the terms of the Creative Commons Attribution 4.0 licence. Any

further distribution of this work must maintain attribution to the author(s) and the title of the work, journal citation and DOI.

¹ Institute of General Electrical Engineering, University of Rostock, Albert Einstein 2, Rostock 18051, Germany

² Institute of Experimental Physics, University of Hamburg, Luruper Chaussee 149, Hamburg 22761, Germany

³ Deutsches Elektronen-Synchrotron, Notkestrasse 85, Hamburg 22607, Germany

⁴ Department Life, Light & Matter, University of Rostock, Albert Einstein 25, Rostock 18051, Germany

^{*} Author to whom any correspondence should be addressed.

1. Introduction

In particle accelerator technology, current radio frequency (RF) resonators are often made of niobium and operated at ultra-low temperatures in the superconducting state to minimize surface losses [1]. For future accelerating structures, surface losses and associated operating costs can be further reduced using new superconducting materials or thin film deposition techniques. In fact, the material properties, surface resistance, and critical RF field predominantly determine the energy consumption and maximum acceleration gradient. Thus, since lower surface resistance results in reduced energy consumption, there is a great need for experiments to determine the superconducting properties of such materials accurately [2–5].

For a precise determination of the RF properties of such superconducting materials, a calorimetric measurement is carried out with the aid of a so-called quadrupole resonator (QPR). The studied QPR was initially developed at CERN in 1997 by [7] to conduct high-precision surface-resistance measurements of niobium samples. Later on, its design was further adapted to operating frequencies of 433 MHz, 866 MHz, and 1.3 GHz at the Helmholtz–Zentrum Berlin [3]. More recently, the HZB configuration has been further modified, amongst others, to overcome existing problems with the influence of microphonics and Lorentz force detuning on measurements bias [8, 9].

A fundamental issue inherent to the existing configurations of QPRs is the measurement bias observed in the third operating mode of the given HZB-QPR (in the range of 1.3 GHz). To illustrate, the $R_S(T)$ measurement data obtained from a bulk niobium sample is presented in figure 3 for all three QPR operating modes with an RF field level of $B_{\text{sample}} = 10 \,\text{mT}$. The unexpectedly high surface resistance measured at 1286 MHz is evident when compared to the measurements provided for other modes, see [11, 12]. Besides the RF losses on the adapter flange [6, 13], microphonics and Lorentz force (LF) detuning [11, 14–16] may constitute the possible explanation of this negative phenomenon. More precisely, according to Slater's theorem [17], any deformation of the cavity shape, for example, due to an external or RF field pressure, could result in the detuning of the resonance frequency [3]. Consequently, mechanical oscillations (microphonics) can be triggered due to the strong LF, especially in the high-field region at the bottom end of the quadrupole rods that break the quadrupole symmetry of the resonator [11, 18]. As a result, due to the relatively small frequency distance between the third quadrupole mode and the closest dipole mode, the closest neighboring mode can be excited [6]. As an illustration of this phenomenon, we present the measurement data obtained when a neighboring dipole mode was simultaneously excited at 1287 MHz (waveform #12 in figure 4). This observation was made during pulsed measurements at the frequency of the third operating mode. Ultimately, this could yield significantly increased RF losses on the bottom stainless steel flange, which might be the probable explanation for the larger measurement bias of the surface resistance for the third quadrupole mode [12].

The QPR consists of a screening cavity made of two thermally isolated chambers and four rods, which are welded at the top plate and bent at the end into half-ring pole shoes, as shown in figure 1. The calorimetry chamber is mounted below these two loops. The resulting power dissipation caused by eddy currents is measured by temperature probes installed inside the calorimetry chamber with a proportional-integral-derivative controller as

$$\Delta P_{\text{RF}}(\mathbf{p}) := [P_{\text{DC1}}(\mathbf{p}) - P_{\text{DC2}}(\mathbf{p})], \tag{1}$$

where $P_{\rm DC1}$ and $P_{\rm DC2}$ denote the heater power required for temperature stabilization at the initial temperature $T_{\rm int}$ and the reduced heater power $P_{\rm DC2}$ determined after switching on the RF antenna and reaching again equilibrium for $T_{\rm int}$, as depicted in figure 2, respectively. Thus, the surface resistance can be calculated using the calorimetric RF-DC-compensation method and reads as

$$R_{S}(\mathbf{p}) = \frac{2\Delta P_{RF}(\mathbf{p})}{\int_{\Omega_{S}} |\mathbf{h}(\mathbf{p})|^{2} d\mathbf{x}},$$
 (2)

with the magnetic field strength as a function of geometrical parameters denoted by $\mathbf{h}(\mathbf{p})$, where the integral term appearing in the denominator of equation (2) is approximated numerically. Specifically, it is a product of a simulation constant c and the stored energy U in the cavity, which is measured using a pickup antenna. For details, we refer to [2, 7]. As a result, the surface resistance is prone to various sources of uncertainties associated with the RF-DC-compensation methodand those resulted from surface treatment methods affecting the surface roughness of superconductors [4].

In particular, the accuracy of the surface resistance measurement, which is determined by both the uncertainty in the RF measurement and the manufacturing imperfections, is of key importance. Specifically, microphonics and LF detuning seem problematic for the operation of the QPR since they directly affect the stability of the resonance field excited by the RF source and, consequently, lead to biased measurements [3]. Also, the static LF detuning can be a key negative factor because it may enlarge the risk of excitation of neighboring modes for some configurations of the QPR [6, 11], for example, the CERNII-QPR design [19]. Besides mechanical vibrations and the LF detuning, manufacturing tolerances deteriorate the QPR's performance [3, 18]. Mathematically, uncertainties related to the physical domain, material coefficients or boundary conditions naturally affect the boundary value problems (BVP) under consideration.

The main problem we face here is to develop a robust and reliable method to measure the impact of a relatively small deformation caused by the LF detuning and the hydrostatic pressure onto suitably chosen merit functions. Its further application is the efficient optimization of QPR design under

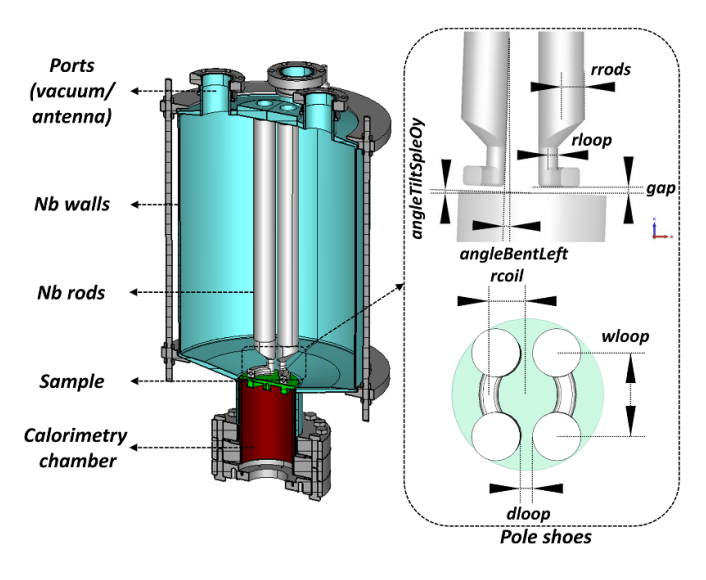


Figure 1. Layout of the QPR (left) with its parameterized model (right). Reproduced from [6]. CC BY 3.0.

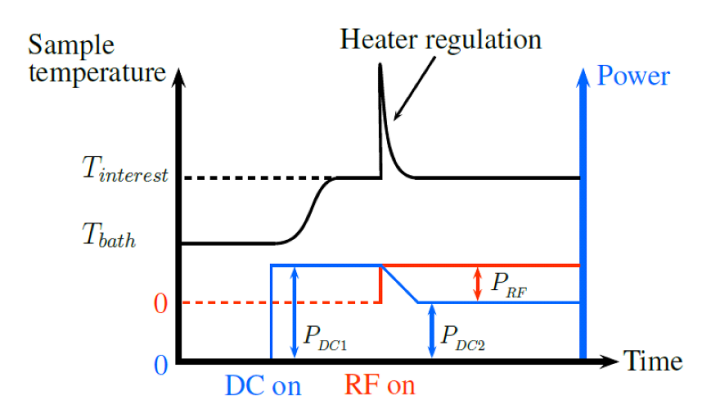


Figure 2. According to the calorimetric method, the surface resistance of a superconducting sample is derived from a DC measurement. Reproduced from [10]. CC BY 3.0.

uncertainty⁵ We note that the standard finite element analysis (FEA) with dynamic re-meshing of the perturbed computational domain may yield a biased solution due to the numerical noise associated with re-meshing, and data transfer [25]. In addition to the boundary representation problem, the mathematical and software limitations⁶ can hinder the use of the FEA for studying small nonlinear deformations.

Although we present a particular application of the QPR model, the proposed approach is general and can be applied to stochastic multi-physics modeling devices such as multicell cavities or couplers from accelerator physics [1, 15, 23]. A comparable approach focusing on the worst-case scenario for an elliptic partial differential equation (PDE) and without

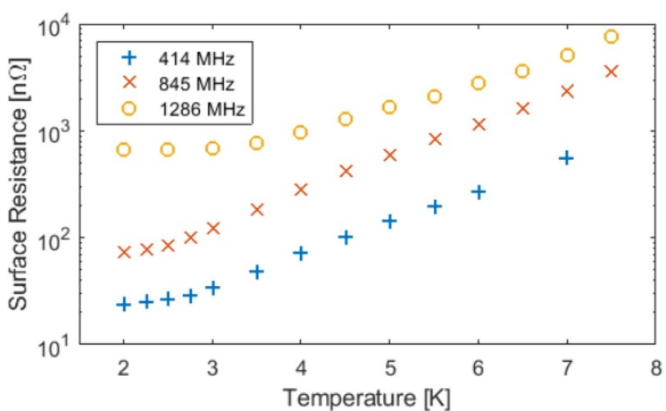


Figure 3. Measurements of $R_S(T)$ conducted for the frequencies of HZB-QPR's three operating modes. Reproduced from [11]. CC BY 3.0.

employing the UQ technique, has been previously explored, e.g. in [27, 28]. In turn, Harbrecht [24] developed a deterministic measure of robustness using the perturbation method with respect to material coefficients. In the context of finance mathematics, the worst-case-expectation formulation for optimizing data processes under uncertainties has been studied in [29]. Moreover, the work presented in [30, 31] addresses certain aspects of the shape derivative for Maxwell's eigenproblem, from a deterministic perspective in a mathematically rigorous manner. The optimization problem constrained by the stochastic formulation of Maxwell's eigenproblem has been successfully studied in our previous work [6, 23].

This paper presents a novel approach to uncertainty quantification analysis and shape perturbation methods, combining them in a worst-case-expectation framework. This approach offers a viable alternative to the method proposed in [25], which employs either a continuum Lagrangian sensitivity analysis or a Monte Carlo method to simulate stochastic phenomena. The proposed adjoint-based *a posteriori* scheme derives the approximation of an upper bound on the deformation caused by the LF radiation and hydrostatic pressure under geometric uncertainty. In this respect, we apply the material and shape derivative to the nonlinear stochastic Maxwell's eigenvalue problem (MEVP) and derive a shape sensitivity in the continuous form. Focusing on this approach, we also address the algorithmic efficiency related to the developed estimations.

2. Stochastic physical model

This section briefly discusses a three-dimensional (3D) mathematical model of the QPR governed by the weakly coupled electro-stress-heat (E-S-H) problem in a deterministic and stochastic setting.

2.1. A deterministic model of QPRs

Suppose our weakly coupled E-S-H BVP is defined on $D \subset \mathbb{R}^d$, d=3, a bounded and simply connected physical domain with sufficiently smooth boundary ∂D . In essence, the boundary can be decomposed into two parts: a Neumann part Γ_N

⁵ Even though the proposed approach for manufacturing processes representation is quite general [20, 21], we prefer the robust formulation, consisting of the expectation's weighted functions and the standard deviation as in [18, 22–24].

⁶ In the CST Studio Suite®—software used for our simulations—a shape sensitivity analysis is implemented only for built-in functions like frequency [26].

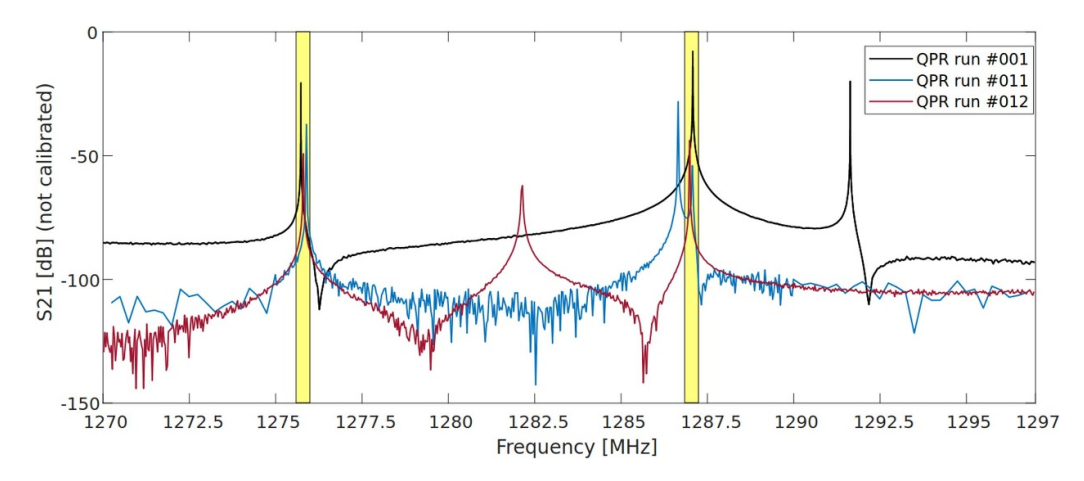


Figure 4. RF mode scans for three distinct measurements with varying samples. The resonant frequency of the third QPR mode exhibits a notable shift of up to 9.2 MHz, while neighboring modes remain in a relatively narrow range of 400 kHz, as highlighted by the yellow areas, see [11, 12]. Reproduced from [11]. CC BY 3.0.

and a Dirichlet part Γ_D such that $\partial D = \Gamma_N \cup \Gamma_D$, which results directly from a multiphysics QPR model, that is, the structure's fixed point, the influence of the helium, and the vacuum pressure and gravitation. In addition, a loss-free material is assumed for modeling the outer cavity, which implies imposing the perfect conducting boundary condition (PEC) on these walls. In fact, we aim to find the eigenpair (λ, \mathbf{h}) comprised of eigenvalue $\lambda \in \mathbb{R}^+$ and the magnetic field phasor $\mathbf{h} \in \mathbb{C}^d$, the vector-valued mechanical displacement $\mathbf{u} \in \mathbb{R}^d$, and the temperature $T \in \mathbb{R}$, which satisfy the coupled system of PDEs consisting of MEVP, the linearized elasticity value problem (EVP), and the heat value problem (HVP). For this reason, let $\mathbf{p} = (p_1, \dots, p_P)^{\top} \in \Pi \subset \mathbb{R}^P$ denote a vector of geometrical parameters with a multidimensional parameter domain given by Π . For example, let us consider these variables, shown in figure 1. Next, define a set of admissible shapes such that

$$\Omega(\mathbf{p}) = \left\{ \mathbf{p} \in \Pi \,\middle|\, \mathbf{0} \leqslant \mathbf{p}_{\min} \leqslant \mathbf{p} \leqslant \mathbf{p}_{\max} \right\},\tag{3}$$

with inequalities understood component-wisely in order to investigate the coupled E-S-H problem.

Then, the variational form of the coupled E-S-H multiphysics problem in the steady-state is: Find $(\lambda, \mathbf{h}) \in \mathbb{R}^+ \times [H^1(D)]^3$ and $\mathbf{h} \not\equiv 0$, $\mathbf{u}, T \in V$ such that

$$\left\langle \mu_r^{-1} \nabla \times \mathbf{h}, \nabla \times \boldsymbol{\varphi} \right\rangle_{D_{\rm c}} - \lambda \left\langle \epsilon_r \mathbf{h}, \boldsymbol{\varphi} \right\rangle_{D_{\rm c}} = 0, \tag{4a}$$

$$\langle \nu \left(\nabla \mathbf{u} + \nabla \mathbf{u}^{\top} \right) + \eta \left(\nabla \cdot \mathbf{u} \right) \mathbf{I}, \nabla \boldsymbol{v} \rangle_{D_{w}} = 0,$$
 (4b)

$$\left\langle \kappa \nabla T, \nabla \vartheta \right\rangle_{D_{\mathbf{w}}} - \left\langle \frac{\gamma}{\epsilon \omega} |\nabla \times \mathbf{h}|^2, \vartheta \right\rangle_{D_{\mathbf{w}}} = 0, \tag{4c}$$

with the LF radiation pressure imposed on the boundary of the rods

$$\langle \boldsymbol{\sigma}, \mathbf{n} \rangle_{\partial D_{\mathrm{cw}}} = \tfrac{1}{4} \left\langle \tfrac{1}{\omega} |\nabla \times \mathbf{h}|^2 + \mu |\mathbf{h}|^2, \mathbf{n} \right\rangle_{\partial D_{\mathrm{cw}}}, \tag{4d}$$

which is satisfied for all $\varphi, v, \vartheta \in V$ with the Sobolev space of functions with square integrable weak gradients denoted

by $V = [H^1(D)]^n$, $n = \{3,1\}$. For example, we have n = 3 in the case of the MEVP and the elasticity equation, that is, (4a) and (4b), while n = 1 for the heat equation of (4c). Similarly, the subspaces $V_g \subset V$ and $V_0 \subset V$ of functions that satisfy the non-homogeneous or homogeneous Dirichlet boundary condition on $\Gamma_D \subset \partial D$ are given by $V_g = H^1_{\Gamma_D} \equiv \{v \in V : v = g \text{ on } \Gamma_D\}$, and $V_0 = H^1_{\Gamma_D} \equiv \{v \in V : v = 0 \text{ on } \Gamma_D\}$, respectively.

In (4a)–(4d), $\omega=2\pi f\in\mathbb{R}^+$ denotes the angular frequency with f standing for the frequency, $\mu\in L^\infty(D)$ the magnetic permeability, and $\epsilon\in L^\infty(D)$ the complex electric permittivity, respectively. The thermal conductivity $\kappa\in L^\infty(D)$ and the electric conductivity $\gamma\in L^\infty(D)$ are real-valued functions. Next, we assume Hooke's law between the linearized Cauchy–Green strain tensor $\varepsilon(\mathbf{u})=\frac{1}{2}\left(\nabla\mathbf{u}+\nabla\mathbf{u}^\top\right)$ and the Cauchy stress tensor C, which in our work is modeled to be independent of the displacement \mathbf{u} . Thus, finally, the stress tensor denoted by $\sigma=C\cdot\varepsilon(\mathbf{u})$ consists of 12 (out of 36 elements) non-vanishing functions of the Lamé coefficients $\eta\in L^\infty(D)$ and $\nu\in L^\infty(D)$ for the considered homogeneous and isotropic material.

Various variants and specializations of the particular PDE associated with the coupled E-S-H problem (4a)–(4d) have been studied for their existence in a deterministic setting. For instance, the uniqueness and solvability of (4a) for simple and multiple eigenvalues⁷ have been shown in [33–35]. Recently, sufficient and necessary conditions to guarantee the uniform convergence of the MEVP have been analyzed in an abstract setting in [36, 37]. Two other elliptic PDE models of (4b) and (4c) for the steady-state of the heat and elasticity equation with loading terms such as the LF pressure and Jules losses, exported from the MEVP and defined at the boundaries of the $\Gamma_{\rm N} \subset \partial D$ and conductive parts of the $\Gamma_{\rm D} \subset \partial D$ flange have been studied in [38, 39]. In particular, the existence and

⁷ Please note, if λ is not an eigenvalue of the homogeneous Dirichlet value problem (homogeneous Neumann problem) with $\mathbf{n} \times \mathbf{h} = 0$ ($\mathbf{n} \times (\mathbf{n} \times \mathbf{h}) = 0$) on the boundary Γ, the solution of (4a) is uniquely determined by $\mathbf{n} \times \mathbf{h} = \mathbf{f}$ ($\mathbf{n} \times (\mathbf{n} \times \mathbf{h}) = \mathbf{g}$), see, e.g. [32].

uniqueness of their solution have been shown, for example, in [27, 28].

Since the manufacturing tolerances and properties of the material used for the QPR determine its functioning, we formulate the stochastic coupled E-S-H problem in the steadystate to achieve reliable simulation results.

2.2. A stochastic coupled E-S-H problem

Following the theory [40–42], let uncertainties associated with geometrical imperfections be represented by the random process $\mathbf{p}(\boldsymbol{\xi})$, defined on the complete probability space $(\mathcal{A}, \mathcal{F}, \mathbb{P})$. Here, \mathcal{A} is an outcome space, $\mathcal{F} \subset 2^{\mathcal{A}}$ denotes the σ -algebra of events, and $\mathbb{P}: \mathcal{F} \to [0,1]$ is a probability measure, respectively. Next, suppose the random field can be approximated by a finite number of random variables $\mathbf{p}(\boldsymbol{\xi}) = (p_1(\xi_1), \dots, p_P(\xi_Q))$ with mutually independent components such that $p_i(\boldsymbol{\xi}): \mathcal{A} \to \Gamma_i \subseteq \mathbb{R}^+$. Specifically, we assume that each random variable is characterized by a probability density function (PDF) $\rho_i: \Gamma_i \to [0,1]$. Furthermore, denote by $\Gamma:=\prod_{i=1}^P \Gamma_i \subset \mathbb{R}^P$ the support of $\mathbf{p}(\boldsymbol{\xi})$ and by

$$\rho(\mathbf{p}) := \prod_{i=1}^{p} \rho_i(p_i)$$

its joint PDF, assuming it exists. Here, the dependence of ξ has been suppressed for better readability.

Then, given the joint PDF $\rho(\mathbf{p})$ of $\mathbf{u}(\mathbf{p}) \in L^2(\Gamma) = \mathbf{u}(\mathbf{p})$: $\mathbb{E}[\|\mathbf{u}(\mathbf{p})\|^2] < \infty\}$, see, [43], the expected value of $\mathbf{u}(\mathbf{p})$ reads

$$\mathbb{E}[\mathbf{u}(\mathbf{p})] := \int_{\Gamma} \mathbf{u}(\mathbf{p}) \, \rho(\mathbf{p}) \, d\mathbf{p}, \tag{5}$$

with the probability measure $\rho(\mathbf{p})d\mathbf{p}$ on Γ .

Similarly, an inner product for two random processes ${\bf u}({\bf p}), {\bf v}({\bf p}) \in L^2(\Gamma)$ is given by

$$(\mathbf{u}(\mathbf{p}), \boldsymbol{v}(\mathbf{p}))_{L_{\rho}^{2}(\Gamma)} := \int_{\Gamma} \mathbf{u}(\mathbf{p}) \cdot \overline{\boldsymbol{v}(\mathbf{p})} \rho(\mathbf{p}) d\mathbf{p}, \quad (6)$$

where $v(\mathbf{p})$ denotes the complex conjugate. The associated norm is then defined as

$$\|\mathbf{u}(\mathbf{p})\| := \left(\int_{\Gamma} \|\mathbf{u}(\mathbf{p})\|^2 \rho(\mathbf{p}) d\mathbf{p}\right)^{\frac{1}{2}}.$$
 (7)

Subsequently, using (5) yields the variance definition of a random complex function $\mathbf{u}(\mathbf{p}) \in L^2(\Gamma)$

$$\operatorname{Var}\left[\mathbf{u}\left(\mathbf{p}\right)\right] := \mathbb{E}\left[\left\|\mathbf{u}\left(\mathbf{p}\right)\right\|^{2}\right] - \left\|\mathbb{E}\left[\mathbf{u}\left(\mathbf{p}\right)\right]\right\|^{2}, \tag{8}$$

which is always real and positive.

Additionally, with regards to a spatial domain $D \subset \mathbb{R}^d$, we define a set of random processes $f(\cdot, \mathbf{p}) : D \to \mathbb{C}^d$, for which a norm on the tensor space $V_\rho = L^2(\Gamma) \otimes H^1_0(D)$ reads as

$$\mathbb{E}\left[\left\|\boldsymbol{f}(\mathbf{x},\mathbf{p})\right\|_{L^{2}(D)}^{2}\right] := \left(\mathbb{E}\left[\int_{\Omega} \|\boldsymbol{f}\|^{2} d\mathbf{x}\right]\right)^{\frac{1}{2}}, \quad (9)$$

which is induced by the corresponding tensor inner product $(\cdot, \cdot)_{V_{-}}$, see, for example, [44, 45].

Let us consider now the tensor product Hilbert space V_{ρ} endowed with the inner product $(\mathbf{u}, \boldsymbol{v})_{V_{\rho}} \equiv \mathbb{E}\left[\langle \mathbf{u}, \boldsymbol{v} \rangle_{V}\right]$ with respect to the stochastic coupled E-S-H problem of (4a)–(4d). Thus, the weak form includes now expectations of the variational form defined in the physical space and it is defined as follows: Find $(\lambda, \mathbf{h}) \in \mathbb{R}^+ \times V_{\rho}$ and $\mathbf{h} \not\equiv 0$, $\mathbf{u}, T \in V_{\rho}$ such that

$$\mathbb{E}\left[\left\langle \mu_r^{-1} \nabla \times \mathbf{h}, \nabla \times \boldsymbol{\varphi} \right\rangle_{D_c} - \lambda \left\langle \epsilon_r \mathbf{h}, \boldsymbol{\varphi} \right\rangle_{D_c}\right] = 0, \quad (10a)$$

$$\mathbb{E}\left[\left\langle \nu\left(\nabla\mathbf{u}+\nabla\mathbf{u}^{\top}\right)+\eta\left(\nabla\cdot\mathbf{u}\right)\boldsymbol{I},\nabla\boldsymbol{\upsilon}\right\rangle _{D_{\mathbf{w}}}\right]=0,\ \ (10b)$$

$$\mathbb{E}\left[\left\langle \kappa \nabla T, \nabla \vartheta \right\rangle_{D_{\mathbf{w}}} - \left\langle \frac{\gamma}{\epsilon \omega} | \nabla \times \mathbf{h}|^2, \vartheta \right\rangle_{D_{\mathbf{w}}}\right] = 0, \quad (10c)$$

equipped with the LF pressure on the boundary of the rods

$$\mathbb{E}\left[\left\langle \boldsymbol{\sigma}, \mathbf{n} \right\rangle_{\gamma}\right] = \mathbb{E}\left[\frac{1}{4} \left\langle \frac{1}{\omega} |\nabla \times \mathbf{h}|^{2} + \mu |\mathbf{h}|^{2}, \mathbf{n} \right\rangle_{\gamma}\right] \quad (10d)$$

with $\gamma = \partial D_{cw}$ for all test functions $\varphi, \upsilon, \vartheta \in V_{\rho}$.

In our work, we employ the non-intrusive approach by Xiu [46] for the solution of (10a)–(10d) to be exploited on a finite-dimensional stochastic subspace $P(\Gamma) \subset L^2(\Gamma)$. For the construction of the approximating $P(\Gamma)$, we adopt a generalized polynomial chaos technique [47–49].

2.3. UQ via polynomial chaos expansion

Given a square-integrable, random function with finite variance $f \in L^2(\Gamma)$, let us consider a truncated series of PC expansion [46, 47, 50] in the following form

$$f(\mathbf{p}) \doteq \sum_{i \in \mathcal{I}_{\Omega, \mathbf{p}}} \widetilde{f}_i \Phi_i(\mathbf{p}), \quad \widetilde{f}_i \in \mathbb{C},$$
 (11)

where i is a multi-index $i = (i_1, ..., i_Q) \in \mathcal{I}_{Q,P}$ with the total polynomial order denoted by P and the set of multi-indices defined as

$$\mathcal{I}_{\mathcal{Q},P} = \left\{ oldsymbol{i} = (i_1, \dots, i_{\mathcal{Q}}) \in \mathbb{N}_0^{\mathcal{Q}} : |oldsymbol{i}| \leqslant P
ight\}$$

with l_1 norm denoted by $|\cdot| := i_1 + ... + i_Q$ and Q related to the number of random variables in the problem. In particular, in (11), the multivariate PC basis functions $\Phi_i(\mathbf{p}) : \mathbb{R}^Q \to \mathbb{R}$ are generated via [20, 51]

$$\Phi_{i}(\mathbf{p}) = \prod_{k=1}^{Q} \Phi_{i_{k}}(p_{k}), \quad i \in \mathcal{I}_{Q,P}$$
(12)

with univariate polynomials of degree $i_k \in \mathbb{N}_0$ to be orthonormal with respect to the L^2_ρ inner product given by (6) and a priori unknown coefficient functions $\widetilde{f_i}$ to be determined.

Correspondingly, we have that the number K of PC basis functions of total order P in dimension Q satisfies

$$K = |\mathcal{I}_{Q,P}| = \frac{(P+Q)!}{P!O!}.$$

A popular choice for the functions Φ_{i_k} are orthonormal polynomials⁸, whose distribution is determined by the description of random variables in stochastic settings. For example, the uniform distribution results in using the Legendre polynomials, whereas the Hermite polynomials correspond to the Gaussian-type PDF, respectively.

In essence, it can be proved that the truncated series of PC expansion given in (11) is convergent in the mean-square sense under the following conditions [40, 41, 50]:

- The variance of $f(\mathbf{p}) \in L^2(\Gamma)$ is finite,
- The coefficients of the PC expansion \widetilde{f}_i can be computed through the so-called projection equation

$$\widetilde{f}_{i} := (f(\mathbf{p}), \Phi_{i}(\mathbf{p}))_{L_{o}^{2}(\Gamma)} = \mathbb{E}[f(\mathbf{p})\Phi_{i}(\mathbf{p})].$$
 (13)

The projection equation constitutes the origin of two main UQ methods: the spectral Galerkin method [48] and the PC-based stochastic collocation method (PC-SCM) [46] (also called pseudo-spectral approach). In our work, the latter (PC-SCM) is preferable due to the possibility of reusing existing deterministic solvers.

2.4. Pseudo-spectral approach

The PC-SCM [46] applies the projection equation only to output interest quantities and yields exponential convergence under certain assumptions on smoothness [47]. In fact, as a typical non-intrusive method, it requires only repetitive simulations of a deterministic model of (10a)–(10d) at a collection of collocation points (cubature nodes) $\mathbf{p}^{(k)} \in \Gamma, k = 1, \dots, K$. Consequently, the discrete projection of resulting solutions $f(\mathbf{p}^k)$ on the basis of polynomials Φ_i can be performed using the multi-dimensional quadrature with associated weights w_k

$$\widetilde{f}_{i} \doteq \sum_{k=1}^{K} w_{k} f\left(\mathbf{p}^{(k)}\right) \Phi_{i}\left(\mathbf{p}^{(k)}\right),$$
(14)

which permits an evaluation of the probabilistic integrals (13).

Likewise, a global approximation of (5), and (8) can be directly carried out when the order of the cubature rule is sufficiently high [52]:

$$\mathbb{E}\left[f(\mathbf{p})\right] = \sum_{k=1}^{K} w_k f\left(\mathbf{p}^{(k)}\right),\tag{15a}$$

$$\operatorname{Var}\left[f(\cdot)\right] = \sum_{k=1}^{K} w_k f^2\left(\mathbf{p}^{(\mathbf{k})}\right) - \left(\sum_{k=1}^{K} w_k f\left(\mathbf{p}^{(k)}\right)\right)^2, (15b)$$

where w_k and $\mathbf{p}^{(k)}$ denote the weights and quadrature nodes, respectively.

Once the polynomial coefficients are found, the polynomial representation in the form of the response surface model (11) allows for estimating

$$\mathbb{E}\left[f(\mathbf{p})\right] = \tilde{f}_{\mathbf{0}}, \quad \text{Var}\left[f(\mathbf{p})\right] = \sum_{i \in \mathcal{I}_{Q,P} \atop i \neq 0} \left|\tilde{f}_{i}\right|^{2}, \tag{16}$$

where $\Phi_0 = 1$. Moreover, given the PC expansion (11) of random variable **p**, other statistical information such as the PDF, the cumulative PDF, or quantities like the local sensitivity and the variance-based global sensitivity can be computed directly; see, for example, [50]. For instance, the local sensitivity (a partial derivative) is defined by

$$\mathbb{E}\left[\frac{\partial f}{\partial p_q}\right] \doteq \sum_{i \in \mathcal{I}_{Q,P}} \left(\tilde{f}_i \int \frac{\partial \Phi_i(\mathbf{p})}{\partial p_q} \rho d\mathbf{p}\right), \tag{17}$$

for q = 1, ..., Q.

The Sobol decomposition of (11), in turn, allows for evaluating the first-order variance-based sensitivity (VBS) coefficients [53]

$$\mathbf{S} = (s)_{l,q} \in \mathbb{R}^{L,Q}, \quad s_{l,q} = \frac{1}{\operatorname{Var}(f_l(\mathbf{p}))} \sum_{i \in I_q} |\tilde{f}_{l,i}|^2, \quad (18)$$

where sets are given by $I_q = \{i \in \mathbb{N}_0 : i_q > 0, i_{m \neq q} = 0\}$ and $\operatorname{Var}(f_l)$ denotes the total variance of particular objective functions, $l = 1, \ldots, L$. Thus, to calculate the first-order VBS $s_{l,q}$, it is required that all random inputs except p_q have to be fixed. Within this concept, a large contribution to the variance is denoted by a value close to 1. In contrast, a value close to 0 indicates a small contribution, which in practice means that the influence of that variable can be neglected either in optimization or in stochastic modeling [6]. The calculation of the total or mixed/fractional VBS coefficients is also possible [54].

The main computational cost of the PC-SCM is associated with using the multi-dimensional quadrature, which determines the number of deterministic solver evaluations at collocation points. Therefore, to overcome the so-called curse of dimensionality caused by employing the Gauss–Hermite (GH) quadrature, typically, the Smolyak approach [55] is recommended, which exploits smooth directions of the random space very robustly [20]. Alternatively, the efficient Stroud formulas can be used [18, 56, 57], which yields a very small number of quadrature points, but they have also a fixed accuracy and cannot be nested. In contrast to the GH rules, other approaches provide nestedness, such as the Newton–Cotes formulas, the Gauss–Patterson or the Clenshaw–Curtis quadrature, and the Hermite Genz–Keister Sparse Grids [45, 57].

3. Shape and material derivative for worst-case approach

A shape derivative is a tool that allows for analyzing the shape variations of domain-dependent quantities $F(\Omega(\mathbf{p}))$, see

⁸ For an orthogonal system of basis polynomials, normalization can be conducted straightforwardly, see, for example, [50].

[58, 59]. Its broad application varies from shape optimization, through the problems of front tracking and image segmentation to *a posteriori* error estimation; see, for example, [60–62].

In particular, given that we are dealing with the third eigenvalue, it is assumed to be simple, and, therefore, shape-differentiable [58, 61].

3.1. Cost functionals

In general, the accuracy of the calorimetric RF-DC-compensation method is affected by (i) manufacturing imperfections, including the roughness of the superconducting surfaces, (ii) a lack of parallelism of the sample surface and the quadrupole pole, (iii) and finally, an insufficient concentric alignment of the coaxial structure [3, 6, 12]. Some of them are clearly design-dependent and can be quantified using the functional

$$\psi\left(\Omega\left(\overline{\mathbf{p}}\right)\right) = F\left[\Omega\left(\overline{\mathbf{p}}\right), \boldsymbol{u}\left(\Omega\left(\overline{\mathbf{p}}\right)\right)\right], \forall \Omega\left(\overline{\mathbf{p}}\right) \in \Pi,\tag{19}$$

assuming that $F(\cdot)$ depends on the parametric shape $\Omega(\mathbf{p})$ implicitly through the solution $\boldsymbol{u}(\Omega(\overline{\mathbf{p}}))$ or explicitly by Ω .

For this reason, to assess the operation of the QPR for the third frequency mode, we consider the following random-dependent cost functionals with $\mathbf{h}_{\Omega} \equiv \mathbf{h}(\mathbf{p})$ and $\Omega(\mathbf{p}) \equiv \Omega$:

- The nominal frequency of the third QPR operating mode⁹:

$$\mathbb{E}\left[f_0\left(\Omega\right)\right] := 1.311 \equiv F_0\left(\Omega\right) \text{ [GHz]}, \qquad (20a)$$

- The focusing factor for investigating the focus of the magnetic field onto the surface of sample Ω_S :

$$\mathbb{E}\left[f_{1}\left(\Omega\right)\right] := \mathbb{E}\left[\frac{1}{2U}\int_{\Omega_{S}}\left\|\mathbf{h}\left(\mathbf{p}\right)\right\|^{2} d\mathbf{x}\right] \equiv F_{1}\left(\Omega, \mathbf{h}\right) \quad (20b)$$

with resulting unit $[MA^2J^{-1}]$.

- The homogeneity factor for measuring the homogeneity of the magnetic field on Ω_S :

$$\mathbb{E}\left[f_{2}\left(\Omega\right)\right] := \mathbb{E}\left[\frac{\int_{\Omega_{S}} \left\|\mathbf{h}\left(\mathbf{p}\right)\right\|^{2} d\mathbf{x}}{\left|\hat{h}_{\Omega_{S}}\left(\mathbf{p}\right)\right|^{2}}\right] \equiv F_{2}\left(\Omega, \mathbf{h}\right) \left[1/1\right].$$

- The measure of the field penetrating into the coaxial gap around the sample, which might lead to a measurement bias:

$$\mathbb{E}\left[f_{3}\left(\Omega\right)\right] := \mathbb{E}\left[\frac{\int_{\Omega_{S}} \left\|\mathbf{h}\left(\mathbf{p}\right)\right\|^{2} d\mathbf{x}}{\int_{\Omega_{F}} \left\|\mathbf{h}\left(\mathbf{p}\right)\right\|^{2} d\mathbf{x}}\right] \equiv F_{3}\left(\Omega, \mathbf{h}\right) \left[1/1\right].$$
(20*d*)

- The ratio of the maximum magnetic field on the sample (Ω_S) over the maximum magnetic field on the rods, which affects the maximum attainable field on Ω_S :

$$\mathbb{E}\left[f_4\left(\Omega\right)\right] := \mathbb{E}\left[\frac{\hat{h}_{\Omega_S}\left(\mathbf{p}\right)}{\hat{h}_{\Omega_R}\left(\mathbf{p}\right)}\right] \equiv F_4\left(\Omega, \mathbf{h}\right) \left[1/1\right]. \tag{20e}$$

- The ratio of the maximum magnetic field on Ω_S over the maximum electric field on the rods to lower the risk of field emission caused by high electric fields:

$$\mathbb{E}\left[f_{5}\left(\Omega\right)\right] := \mathbb{E}\left[\frac{\omega\mu_{0}\,\hat{h}_{\Omega_{S}}\left(\mathbf{p}\right)}{\nabla\times\hat{h}_{\Omega_{R}}\left(\mathbf{p}\right)}\right] \equiv F_{5}\left(\Omega,\mathbf{h}\right) \qquad (20f)$$

with resulting unit $[mT(MV/m^{-1})]$,

- The maximum temperature at the adapter flange:

$$\mathbb{E}\left[f_{6}\left(\Omega\right)\right] := \mathbb{E}\left[\hat{T}_{\Omega_{F}}\left(\mathbf{p}\right)\right] \equiv F_{6}\left(\Omega, \mathbf{h}, T\right) \left[T\right], \quad (20g)$$

where $\hat{h} = |\hat{\mathbf{h}}|$ denotes the peak magnetic field that is calculated either in the area of the sample $\Omega_{\rm S}$ or in the domain of the rods $\Omega_{\rm R}$. Here, $\Omega_{\rm F}$ refers to the region of the flange, while U denotes the stored energy in the QPR.

3.2. Shape derivative for quantifying LF influence

In the presence of small deformations of the QPR shape under geometric uncertainties caused by the LF detuning, we can employ a shape perturbation analysis around the nominal parametric shape $\Omega(\mathbf{p}_0)$ to estimate the change of functions (19)

$$\Delta F[\Omega(\overline{\mathbf{p}})] = \sup_{\Omega(\mathbf{p}) \in \Pi} \mathbb{E}\left[\psi(\Omega(\mathbf{p})) - \psi(\Omega(\mathbf{p}_0))\right], \quad (21)$$

which might be understood here as the worst-case average of the objective functional [29].

Furthermore, let us assume that for the fixed realization of quadrature nodes $\mathbf{p}^{(k)}$, merit functions, bilinear and linear forms of (4a)–(4d) are regular functions of the parametric shape $\Omega^{(k)}:=\Omega\left(\mathbf{p}^{(k)}\right)$. Next, suppose $\mathbf{v},\mathbf{w}\in W=C^k(\mathbb{R}^d,\mathbb{R}^d)$ are sufficiently smooth vector (Lipschitz continuous) fields, where W denotes the Banach subspace. Then, the shape derivative $\mathrm{d}\,\psi$ of the functional $\psi\left(\Omega\right)$ evaluated at $\Omega^{(k)}$ is introduced in a weak sense [58]

$$\left\langle \mathbf{d}\psi\left(\Omega^{(k)}\right), \mathbf{v} \cdot \mathbf{n} \right\rangle = \lim_{\tau \to 0^{+}} \frac{\psi\left[T_{\tau}^{\mathbf{v}}\left(\Omega^{(k)}\right)\right] - \psi\left(\Omega^{(k)}\right)}{\tau}, \tag{22}$$

for all $\mathbf{v} \in W$, where $T^{\mathbf{v}}_{\tau}(\Omega)$ represents the transformed domain that is obtained by perturbing the original domain Ω with a certain distance τ in the direction of the vector field \mathbf{v} and \mathbf{n} is the unit outward normal to Ω . Similarly, we can define a shape Hessian of ψ calculated at $\mathbf{p}^{(k)}$; see, for example, [63, 64]

⁹ The difference between the simulated and measured frequencies of HZB-QPR operating modes might be attributed to the frequency tuning of geometrical parameters (ltrans1, ltrans2) to accommodate existing narrow bandwidth RF systems of 400 MHz and 1300 MHz [3, 12]. Indeed, our simulation results align with those reported by other studies on HZB-QPR, see, e.g. [13, 16].

$$\left\langle \mathbf{d}^{2}\psi\left(\Omega^{(k)}\right),\mathbf{v}\otimes\left(\mathbf{w}\cdot\mathbf{n}\right)\right\rangle = \lim_{\tau\to0^{+}}\frac{\mathbf{d}\psi\left[T_{\tau}^{\mathbf{w}}\left(\Omega^{(k)}\right),\mathbf{v}\right] - \mathbf{d}\psi\left(\Omega^{(k)},\mathbf{v}\right)}{\tau},\tag{23}$$

for all $\mathbf{v}, \mathbf{w} \in W$.

Then, for all parametric shapes $\Omega(\mathbf{p}) = \Omega(\mathbf{p}_0 + \delta \mathbf{p}) \in \Pi$ and $\theta \in (0,1)$, the following expansion holds

$$\psi \left[\Omega \left(\mathbf{p}^{(k)} \right) \right] - \psi \left[\Omega \left(\mathbf{p}_0^{(k)} \right) \right] = \left\langle d\psi \left[\Omega \left(\mathbf{p}_0^{(k)} \right) \right], \mathbf{v} \right\rangle + \frac{1}{2} \left\langle d^2 \psi \left[\Omega \left(\mathbf{p}_0 + \theta \mathbf{p} \right)^{(k)} \right], \mathbf{v} \otimes (\mathbf{v} \cdot \mathbf{n}) \right\rangle. \tag{24}$$

Finally, considering (24), we can propose the estimation of the upper bound of the worst-case uncertainty introduced in (19) for the fixed quadrature node $\mathbf{p}^{(k)}$

$$\Delta F \leqslant \sup_{\delta \mathbf{p} \in \Pi} \left| \left\langle d\psi^{(k)} \left(\mathbf{p}_{0} \right), \delta \mathbf{p} \right\rangle \right|$$

$$+ \frac{1}{2} \sup_{\delta \mathbf{p} \in \Pi} \sup_{\delta \theta \in (0,1)} \left| \left\langle d^{2} \psi^{(k)} \left(\mathbf{p}_{0} + \theta \mathbf{p} \right), \delta \mathbf{p}, \delta \mathbf{p} \right\rangle \right|. \quad (25)$$

Next, we can use the shape and material derivative to find the variations of the merit functions caused by the LF radiation and hydrostatic pressure in the continuous framework for the stochastic coupled E-S-H problem in the steady state.

3.3. Material derivative concept

Here, we employ the material derivative concept from continuum mechanics to represent the deformation process as the mapping within the time interval $\tau \geqslant 0$ defined as

$$T_{\tau}: \Omega \subset \mathbb{R}^d \mapsto \Omega_{\tau} \subset \mathbb{R}^d$$
,

where $\Omega \subset D$ and $\Omega_{\tau} \subset D$ denote the (fixed) domain and the perturbed domain, respectively. Furthermore, in the case of sufficiently small τ , let $\Omega_{\tau} \equiv T_{\tau}(\Omega, \tau)$ be the image of the fixed domain Ω , which implies $\mathbf{x}_{\tau} \equiv T_{\tau}(\mathbf{x}, \tau), \mathbf{x} \in \Omega$. For example, when the first-order shape derivative is considered, we get

$$T_{\tau}(\mathbf{x}) = \mathbf{x} + \tau \mathbf{v}(\mathbf{x}), \tag{26}$$

with $\mathbf{v} \in [C^1(\mathbb{R})^d]^d$ and $\mathbf{v} = \mathbf{0}$ on ∂D . Next, for $\mathbf{h} \in [H^1(\Omega)]^d$ and $\mathbf{h}_{\tau} \in [H^1(\Omega_{\tau})]^d$ define the composition $\mathbf{h}^{\tau} = \mathbf{h}_{\tau} \circ T_{\tau}$. Then, if the pointwise material derivative $\dot{\mathbf{h}}$ exists at $\mathbf{x} \in \Omega$, it is defined as

$$\dot{\mathbf{h}}(\mathbf{x}) \equiv \frac{\mathrm{d}}{\mathrm{d}\tau} \mathbf{h}^{\tau} (\mathbf{x} + \tau \mathbf{v}(\mathbf{x})) \Big|_{\tau=0} = \mathbf{h}'(\mathbf{x}) + \mathbf{v}(\mathbf{x}) \cdot \nabla \mathbf{h}(\mathbf{x}),$$
(27)

assuming that $\mathbf{u}^{\tau}(\mathbf{x})$ has a regular extension to a neighborhood of $\overline{\Omega}_{\tau}$. Here, \mathbf{h}' is the partial derivative and $\mathbf{v}(\mathbf{x}) \cdot \nabla \mathbf{h}(\mathbf{x}) = v_j[\partial h_i/\partial x_j]$, as in [58]. In fact, $\dot{\mathbf{h}}$ defined this way only makes sense for a strong formulation. On contrast, the weak solutions require its consideration in the Sobolev norm sense [59].

Furthermore, denote by $DT_{\tau} = Id + \tau \nabla \mathbf{v}(\mathbf{x})$ the Jacobian of (26) and by $I_{\tau} := \det(DT_{\tau})$ its determinant, where $Id = [\delta_{ij}]$ and $\nabla \mathbf{v}(\mathbf{x})$ denote the identity and Jacobian matrix. Other basic material derivative formulas can be found, for example, in [60, 65, 66]. Next, consider the domain-dependent functional as follows

$$\mathcal{J}_{1}\left(\Omega_{ au}
ight)=\int_{\Omega_{ au}}f_{t}(oldsymbol{x}_{ au})\,\mathrm{d}oldsymbol{x}_{ au},$$

with a regular function f_{τ} defined in Ω_{τ} . Then, based on (27) and the definition of I_{τ} , the material derivative of $\mathcal{J}_1(\Omega_{\tau})$ can be derived [58] using first the transformation of the integral domain Ω_{τ} to Ω and next the divergence theorem:

$$d\mathcal{J}_{1} = \frac{d}{d\tau} \int_{\Omega_{t}} f_{t}(\mathbf{x}) d\mathbf{x} \Big|_{t=0} = \frac{d}{d\tau} \int_{\Omega} f^{\tau} (\mathbf{x} + \tau \mathbf{v} (\mathbf{x})) I_{t} d\mathbf{x} \Big|_{\tau=0}$$

$$= \int_{\Omega} \left[f'(\mathbf{x}) + \nabla f(\mathbf{x})^{\top} \mathbf{v} (\mathbf{x}) + f(\mathbf{x}) \nabla \cdot \mathbf{v} (\mathbf{x}) \right] d\mathbf{x}$$

$$= \int_{\Omega} f'(\mathbf{x}) d\mathbf{x} + \int_{\partial\Omega} f(\mathbf{x}) \nu_{n} d\mathbf{x}.$$
(29)

Here, $v_n = \mathbf{v} \cdot \mathbf{n}$ denotes the normal component of the velocity field on the boundary $\partial \Omega$.

Likewise, the material derivative of the boundary functional

$$\mathcal{J}_{2}\left(\Gamma_{\tau}\right) = \int_{\Gamma} g\left(\boldsymbol{x}_{\tau}\right) d\boldsymbol{x}_{\tau}$$

is expressed as

$$d\mathcal{J}_{2} = \int_{\Gamma} \left[g'(\mathbf{x}) + (\nabla g^{\mathsf{T}} \mathbf{n} + \kappa g(\mathbf{x}) v_{n}) \right] d\mathbf{x}, \qquad (30)$$

with $\kappa = \nabla \cdot \boldsymbol{n}$ under assumption that g_{τ} is a regular function defined on Γ_{τ} and the mapping $\mathbf{v} \mapsto \dot{g}$ is linear and continuous [59].

4. Shape sensitivity analysis for stochastic E-S-H problem

In this section, we aim at quantifying the influence of the multiphysics shape deformation caused by the LF radiation pressure on QPR operations. Thus, we employ the material and shape derivative to characterize uncertainty on suitable merit functions in the worst-case average sense of functional outputs.

4.1. Continuous shape derivative for the SMEVP

Without loss of generality, let us consider the robust formulation of merit functions (20) as the weighted sum of (15), that is,

$$F_r(\mathbf{f}_i) = \eta \mathbb{E}(\mathbf{f}_i) + (1 - \eta) \sqrt{\operatorname{Var}(\mathbf{f}_i)}, \quad i = 1, \dots, N, \quad (31)$$

which enables equivalently the study of the hydrostatic and LF radiation pressure impact in the L^2 -norm with respect to

the ellipsoidal uncertainty set [67]. Here, $f_i = \left(f_i^{(1)}, \dots, f_i^{(K)}\right)$ is the collection of the merit functions evaluated at quadrature nodes while $\eta = 1$ permits to retrieve the expectation form as the performance measure.

Furthermore, suppose the expectation/robust function $F_r(f_i)$ is well-defined, finite-valued, continuous, and convex. Then, it is subdifferentiable, which results in commuting the differential with the expectation operator [29]. This yields the weighted shape derivative in the form [68]

$$dF_r(\mathbf{f}_i) = \sum_{k=1}^{K} \alpha_{k,i} dF_i \left[\Omega \left(\mathbf{p}^{(k)} \right) \right], \tag{32}$$

where $dF_i[\Omega(\mathbf{p}^{(k)})]$ denotes a shape derivative with coefficients

$$\alpha_{k,i} = \eta w_k + (1 - \eta) w_k \frac{f_i^{(k)} - \mathbb{E}(f_i)}{\sqrt{\operatorname{Var}(f_i)}}, \tag{33}$$

with quadrature weights denoted by \mathbf{w} as in formulas (15).

In the following, we use $(u,v)_{L^2(\Gamma)\otimes L^2(Y)}=\mathbb{E}\left[\langle u,v\rangle_Y\right]$ to indicate the physical domain Y, which might be a bit ambiguous. Then, following [69, 70], we define the Lagrangians that augment the self-adjoint function (20a) and others (20b)–(20g) by inner products $(\cdot,\cdot)_{V_\rho}$ of $(\zeta_\tau,\varphi_\tau)\in\mathbb{R}\times V_\rho$ with the stochastic MEVP (10a), the normalization and the Neumann boundary condition

$$\mathcal{L}_{0}(\mathbf{h}_{\tau}, \lambda_{\tau}, \boldsymbol{\varphi}_{\tau}, \zeta_{\tau}) = -\mathbb{E}\left[f_{0\tau}\right]$$

$$+ \mathbb{E}\left[\left\langle \epsilon_{r}^{-1} \nabla \times \mathbf{h}_{\tau}, \nabla \times \boldsymbol{\varphi}_{\tau} \right\rangle_{\Omega_{\tau}}\right]$$

$$- \mathbb{E}\left[\lambda \left\langle \mu_{r} \mathbf{h}_{\tau}, \boldsymbol{\varphi}_{\tau} \right\rangle_{\Omega_{\tau}}\right]$$

$$+ \mathbb{E}\left[\frac{\zeta_{\tau}}{2} \left(\left\langle \mu_{r} \mathbf{h}_{\tau}, \mathbf{h}_{\tau} \right\rangle_{\Omega_{\tau}} - 1\right)\right]$$

$$+ \mathbb{E}\left[\left\langle \epsilon_{r}^{-1} \mathbf{n} \times \mathbf{h}_{\tau}, \mathbf{n} \times \boldsymbol{\varphi}_{\tau} \right\rangle_{\partial\Omega_{\tau}}\right], \quad (34)$$

and

$$\mathcal{L}_{2}(\mathbf{h}_{\tau}, \lambda_{\tau}, \boldsymbol{\varphi}_{\tau}, \zeta_{\tau}) = -\frac{1}{2} \mathbb{E} \left[\left\langle \chi_{1} f_{i_{\tau}}, f_{i_{\tau}} \right\rangle_{\gamma} \right]$$

$$+ \mathbb{E} \left[\left\langle \epsilon_{r}^{-1} \nabla \times \mathbf{h}_{\tau}, \nabla \times \boldsymbol{\varphi}_{\tau} \right\rangle_{\Omega_{\tau}} \right]$$

$$- \mathbb{E} \left[\lambda_{\tau} \left\langle \mu_{r} \mathbf{h}_{\tau}, \boldsymbol{\varphi}_{\tau} \right\rangle_{\Omega_{\tau}} \right]$$

$$+ \mathbb{E} \left[\frac{\zeta_{\tau}}{2} \left(\left\langle \mu_{r} \mathbf{h}_{\tau}, \mathbf{h}_{\tau} \right\rangle_{\Omega_{\tau}} - 1 \right) \right]$$

$$+ \mathbb{E} \left[\left\langle \epsilon_{r}^{-1} \boldsymbol{n} \times \mathbf{h}_{\tau}, \boldsymbol{n} \times \boldsymbol{\varphi}_{\tau} \right\rangle_{\partial\Omega_{\tau}} \right], \quad (35)$$

for i = 1,...,I, I = 5 to indicate any functional in the range of $\{f_1,...,f_I\}$ from (20b)–(20f). Here, χ^{10} is a characteristic function, defined as a positive and constant value on $\partial\Omega$, and zero otherwise. The existence of Lagrange multipliers for deterministic/stochastic optimal control problems via shape derivatives is proved, e.g. in [71, 72].

Then, to find stationary points of the Lagrangians and, finally, a shape derivative of functionals, we consider variations of \mathcal{L}_0 and \mathcal{L}_2 with respect to adjoint and state eigenpairs by using the material derivative given by (28) and (30). This leads to

$$d\mathcal{J}_{0}\left[f_{0}\left(\mathbf{p}\right)\right] = \sum_{k=1}^{K} \alpha_{k,0} dF_{i}^{(k)}\left(\mathbf{p}\right)$$
(36a)

with

$$dF_{i}^{(k)} = \left\langle \epsilon_{r}^{-1} \nabla \times \boldsymbol{u}^{(k)}, \nabla \times \boldsymbol{\varphi}^{(k)} v_{n}^{(k)} \right\rangle_{\gamma} - \lambda \left\langle \mu_{r} \boldsymbol{u}^{(k)}, \boldsymbol{\varphi}^{(k)} v_{n}^{(k)} \right\rangle_{\gamma}$$
(36b)

where the coefficients $a_{k,i}$ are defined by (33). For $\eta = 1$, a multi-dimensional quadrature rule can be replaced by $\mathbb{E}[\cdot]$. Note that the calculation of d $\mathcal{J}_0[f_0(\mathbf{p})]$ does not require solving the dual problem since the eigenvalue is a self-adjoint quantity [69].

In the case of other functionals, first, we have to formulate the dual problem, which in the weak sense is defined as: For $\phi \in V_{\rho}$ find $(\zeta, \varphi) \in \mathbb{R} \times V_{\rho}$

$$\mathbb{E}\left[\left\langle \epsilon_{r}^{-1} \nabla \times \boldsymbol{\varphi}, \nabla \times \boldsymbol{\phi} \right\rangle - \lambda \left\langle \mu_{r} \boldsymbol{\varphi}, \boldsymbol{\phi} \right\rangle + \zeta \left\langle \mathbf{h}, \mu_{r} \boldsymbol{\phi} \right\rangle\right]$$

$$= -\mathbb{E}\left[\left\langle \epsilon_{r}^{-1} \boldsymbol{n} \times \boldsymbol{\varphi}, \boldsymbol{n} \times \boldsymbol{\phi} \right\rangle_{\gamma}\right]$$

$$+ \sum_{k=1}^{K} \left\langle \chi \alpha_{k,i} D_{\mathbf{h}}, \nabla \times \mathbf{h} \boldsymbol{f}_{i}^{(k)}, \boldsymbol{\phi} \right\rangle_{\gamma}, \tag{37a}$$

with $D_{\mathbf{h}}f_1 \equiv \partial f_1/\partial \mathbf{h}$, $\lambda' = 1$ and $D_{\nabla \times \mathbf{h}}f_1 \equiv \partial f_1/\partial (\nabla \times \mathbf{h})$ for i = 1, ..., I, with the orthogonality condition given by

$$\mathbb{E}\left[\langle \mu_r \mathbf{h}, \boldsymbol{\varphi} \rangle\right] = 0. \tag{37b}$$

Since variations of the Langragian (35) with respect to eigenfrequency λ have been taken into account.

Finally, we conclude that the shape derivative for other functionals from (20b)–(20f) is given by

$$d\mathcal{J}_{i}[f_{i}(\mathbf{p})] = \sum_{k=1}^{K} \alpha_{k,0} dF_{i}^{(k)}(\mathbf{p}), \qquad (38a)$$

where

$$dF_{i}^{(k)}(\mathbf{p}) = \left\langle \epsilon_{r}^{-1} \nabla \times \boldsymbol{u}^{(k)}, \nabla \times \boldsymbol{\varphi}^{(k)} v_{n}^{(k)} \right\rangle_{\gamma}$$

$$- \lambda \left\langle \mu_{r} \boldsymbol{u}^{(k)}, \boldsymbol{\varphi}^{(k)} v_{n}^{(k)} \right\rangle_{\gamma}$$

$$+ \frac{\zeta}{2} \left\langle \mu_{r} \boldsymbol{u}^{(k)}, \boldsymbol{u}^{(k)} v_{n}^{(k)} \right\rangle_{\gamma}$$

$$- \left\langle \chi \boldsymbol{J}_{i}^{(k)}, \boldsymbol{f}_{i}^{(k)} \kappa v_{n}^{(k)} \right\rangle_{\gamma}$$

$$+ \left\langle \epsilon_{r}^{-1} \boldsymbol{n} \times \boldsymbol{u}^{(k)}, \left(\boldsymbol{n} \times \boldsymbol{\varphi}^{(k)} \right) \kappa v_{n}^{(k)} \right\rangle_{\gamma}. \quad (38b)$$

Again, for $\eta = 1$, we can recover the expectation measure. The derivation details are given in appendix.

 $^{^{10}}$ If the functional is defined as a pointwise quantity, then $\langle \chi_1 f_{i_\tau}, f_{i_\tau} \rangle_{\gamma}$ shall involve a Dirac function [58].

In conclusion, we want to point out that shape derivatives defined by (34) and (35) require either the generation of a velocity field or expressing their form as boundary functionals. In principle, there are various approaches to automatically compute \mathbf{v} , each with its pros and cons; see, e.g. [73–75]. However, we aim to explicitly find the relation between variations of the merit functions and changes of the QPR shape due to the LF radiation pressure as in (10a)–(10d). Therefore, inspired by [15], we explicitly associate the velocity field with the displacement $\mathbf{v}^{(k)} = g(\mathbf{u}^{(k)})$ provided by the stochastic EVP (10b) solution 11.

5. Numerical experiments and discussion

The algorithm developed for estimating variations of functionals due to deformations caused by the static LF detuning, as well as atmospheric and helium pressure, has been verified using two test cases, which include an academic benchmark and the design of the QPR under uncertainties.

5.1. Analytical and numerical academic benchmark

As a test case #1, we consider a circular pill-box cavity with PEC boundary and with thin beryllium foils inside as in [76], displayed in figure 5. This example may also be relevant to the QPR design due to the availability of analytical formulas for electromagnetic fields and stresses produced by various sources of pressure or temperature fluctuations [77–79]. The analysis aims to verify the sensitivity formula thanks to existing analytically derived solutions and the fact that geometric uncertainties can be easily included. In addition, we intend to study the effect of the applied quadrature on the resulting solutions. Specifically, the fundamental transverse magnetic mode TM₀₁₀ is of particular interest in accelerator physics since it provides a maximum electric field along the particles' trajectory in the center of the structure. For this mode, the electromagnetic field components are defined as [78]

$$e_z(\mathbf{r},t) = e_0 J_0(kr) e^{i\omega t}, \tag{39a}$$

$$h_{\phi}\left(\mathbf{r},t\right) = i\sqrt{\frac{\epsilon_{0}}{\mu_{0}}}E_{0}\left(kr\right)e^{i\omega t},\tag{39b}$$

with the zth component of the electric field strength denoted by $e_z(\mathbf{r},t)$ and the operational frequency of the TM₀₁₀ mode of the pill-box cavity given by

$$f_{010} = \frac{1}{2\pi\sqrt{\epsilon_0\mu_0}}k_{010},\tag{39c}$$

where the wave number $k_{010} = (\omega/c) = (p_{01}/a) = 2.405/a$, with the *m*th root of zero-order Bessel function J_0 denoted by p_{0m} and a the inner radius of the cavity. Here, e_0 is the maximum attainable electric field.

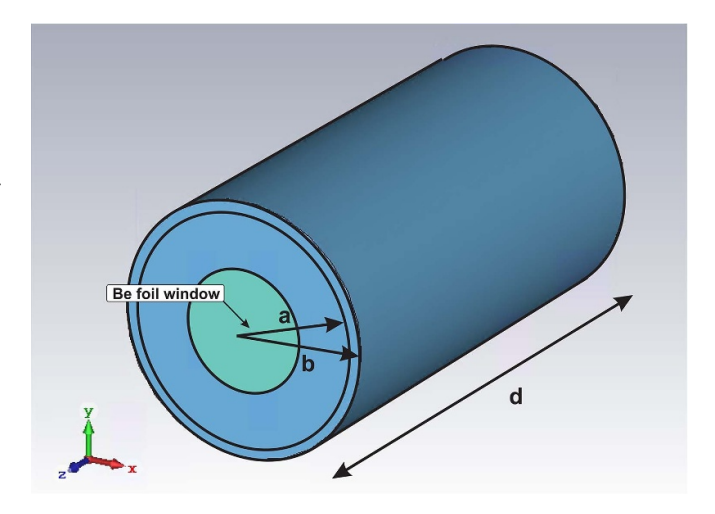


Figure 5. Model of a pill-box cavity with a beryllium window.

Furthermore, the average power loss over one RF period is given by [76]

$$P(r) = \frac{\mu_0 \omega}{2\gamma} \int_0^r h_t \overline{h}_t dr, \tag{40}$$

assuming that only the TM_{010} mode has been excited, which depends only on r due to the circular symmetry. Here, h_t is the tangential component of the magnetic field with the complex conjugate operator denoted by $\bar{\ }$. Then, the temperature distribution in the cylindrical model can be expressed as

$$\frac{\mathrm{d}T(r)}{\mathrm{d}r} = \frac{1}{\kappa a} \left[\frac{1}{r} \frac{\mu_0 \omega}{2\gamma} \int_0^r h_t \overline{h}_t \mathrm{d}r \right],\tag{41}$$

where κ denotes the coefficient of thermal conductivity.

Moreover, considering the thin-walled cylinder $(a/(b-a) \le 10)$, we can find the stress components due to the uniform internal p_{LF} and external pressure p_0 [80]

$$\sigma_r = \frac{a^2b^2(p_0 - p_{LF})}{(b^2 - a^2)r^2} + \frac{p_{LF}a^2 - p_0b^2}{b^2 - a^2},$$
(42)

$$\sigma_{\theta} = -\frac{a^2 b^2 (p_0 - p_{\rm LF})}{(b^2 - a^2)r^2} + \frac{p_{\rm LF} a^2 - p_0 b^2}{b^2 - a^2}.$$
 (43)

Then, the radial displacement is simply given by

$$u_r = \frac{r}{E} \left(\sigma_\theta - \eta \sigma_r \right),\tag{44}$$

with the Young's modulus denoted by *E*. Likewise, displacements due to the heating of the pill-box cavity can be found [77]. Thus, our benchmark considers the expectation of frequency shift, and average power loss as the quantities of interest. Analogously, the maximum temperature can be analyzed.

Since a cylindrical resonator with PEC boundary represents a simple BVP, the analytical solutions are available to the frequency of TM_{010} mode (39c) and the power losses in the beryllium foils (40) when using (39b). Therefore, the first/second shape derivative can be straightforwardly expressed as the partial derivatives. Then, the shape variation (44) due to the

 $^{^{11}}$ In the same way, the HVP can be considered. However, in our analysis, the effect of thermal expansion is neglected. Instead, we export the Joule losses to solve the stochastic HVP (10c) for the T distribution in the flange.

stresses caused by hydrostatic and LF radiation pressure (42)–(43) and those resulting from geometric uncertainties can be easily involved. Finally, the worst-case upper bound for each quadrature node and then $\Delta \mathbb{E}[\psi]$ (in L^{∞}) can be quantified using (25), while an ellipsoidal uncertainty set (in L^2) can be approximated by variance (15a) or (16) for a perturbed shape or provided by the first order shape derivative framework, respectively. In the second case, we can calculate a (first order) shape derivative using (36a) or (38), which allows us to find the resulting variations of performance functionals.

For UQ analysis, we have considered three normally distributed random variables $\mathbf{p}(\boldsymbol{\xi})$ such as the inner radius of the pillbox cavity $p_1(\xi_1) = \tilde{\mu}_1(a) + \tilde{\sigma}_1(a)$, the ambient pressure $p_2(\xi_1) = \tilde{\mu}_2(p_0) + \tilde{\sigma}_2(p_0)$, and the LF radiation pressure $p_3(\xi_1) = \tilde{\mu}_3(p_{\rm LF}) + \tilde{\sigma}_3(p_{\rm LF})$ with $\tilde{\mu}(\mathbf{p}) =$ $(0.1426 \text{ [m]}, \mathbb{E}[\sigma_{LF}(\mathbf{h})], 1.6 \text{ [mbar]}) \text{ and } \tilde{\sigma}_i(p_i) = \delta_i \cdot \tilde{\mu}_i(p_i),$ where the magnitude of perturbation is specified as δ_i 0.01, i = 1,2,3 for all the random variables. Furthermore, we employ Hermite polynomials as the basis functions (11) in the PC-SCM, since they form the optimal basis corresponding to Gaussian distribution [50]. Next, to study the influence of the quadrature rule on the resulting approximation of the quantities of interest (13), we have applied the GH quadrature rule and compared the obtained results with those provided by Stroud formulas [56, 57, 81]. More specifically, we have considered Stroud's formulas with the following cubature degree: $K(Q) = Q^2 + Q + 2$ (Stroud-5), $K = 2 \cdot Q$ (Stroud-3), K(Q) = Q + 1 (Stroud-2). The results are listed in tables 1 and 2, respectively.

Finally, it can be summarized that the Stroud-3 cubature rule with relatively low algorithmic complexity but the fixed accuracy (K = 6) compared to the complexity of the GH quadrature rule ($K(Q) \approx Q^3, K = 27$) provides accurate enough results for estimating the functional variations due to the shape deviation.

5.2. Multiphysics QPR model

In this example, we analyze the physical model of the QPR shown in figure 1 with the geometric design parameters listed in Table 3. It is described by a set of PDEs with suitable boundary conditions specified by (10a)–(10d). The QPR's performance is very sensitive to mechanical disturbances due to its design consisting of a cylindrical cavity with long rods attached solely to the top of the top cover. Thus, microphonics and LF detuning are critical issues for the operation of the QPR since, according to Slater's theorem, the deformed cavity shape detunes the resonance frequency of a cavity. To be more specific, the influence of air and static LF radiation pressure is estimated based on measurements as

$$\frac{\partial f}{\partial p} = 2.6 \; (\mathrm{kHz} \, \mathrm{mbar}^{-1}), \quad \frac{\partial f}{\partial B} = 0.96 \; (\mathrm{Hz} \, \mathrm{mT}^{-2}), \label{eq:definition}$$

with $B = |\mu \mathbf{h}|$. These values are about three orders of magnitude above typical values for elliptical cavities [3]. In order to assess the contribution of each sensitivity to explaining the total frequency variation, however, the Taylor-based global

Table 1. Means and f_{010} upper bounds in $\Omega^0(\overline{\mathbf{p}})$ and $\Omega^*(\overline{\mathbf{p}})$ pill-box model^{a.}

model			
Quantity of interest	$F(\Omega^0)$	$F(\Omega^*)$	$\delta [\%]$
Analytical solution			
GH quadrature, $K = 27$ $\mathbb{E}[f_{010}]$ (frequency) [MHz] $\Delta \mathbb{E}[f_{010}]$ [MHz] in L^2 $\Delta \mathbb{E}[f_{010}]$ [MHz] in L^∞	805.08 8.053 11.736	794.77 8.072 11.76	1.280 ↓ 0.238 ↑ 1.93 ↑
	11.750	11.70	1.93
Stroud-5 cubature, $K = 14$ $\mathbb{E}[f_{010}]$ (frequency) [MHz] $\Delta \mathbb{E}[f_{010}]$ [MHz] in L^2 $\Delta \mathbb{E}[f_{010}]$ [MHz] in L^∞	805.08 8.053 10.818	794.77 8.072 11.128	1.280 ↓ 0.238 ↑ 4.78 ↑
Stroud-3 cubature, $K = 6$ $\mathbb{E}[f_{010}] \text{ (frequency) [MHz]}$ $\Delta \mathbb{E}[f_{010}] \text{ [MHz] in } L^2$ $\Delta \mathbb{E}[f_{010}] \text{ [MHz] in } L^\infty$	805.08 8.053 10.709	794.77 8.072 10.748	1.280 ↓ 0.238 ↑ 1.93 ↑
Stroud-2 cubature, $K = 4$ $\mathbb{E}[f_{010}]$ (frequency) [MHz] $\Delta \mathbb{E}[f_{010}]$ [MHz] in L^2 $\Delta \mathbb{E}[f_{010}]$ [MHz] in L^∞	805.08 8.051 10.876	794.77 8.070 10.831	1.280 ↓ 0.24 ↑ 1.06 ↑
First-order shape derivative			
GH quadrature, $K = 27$ $\mathbb{E}[f_{010}]$ (frequency) [MHz] $\Delta \mathbb{E}[f_{010}]$ [MHz] in L^2 $\Delta \mathbb{E}[f_{010}]$ [MHz] in L^∞	805.08 8.053 11.736	794.63 8.068 11.94	1.298 ↓ 0.186 ↑ 1.7479 ↑
Stroud-5 cubature, $K = 14$ $\mathbb{E}[f_{010}] \text{ (frequency) [MHz]}$ $\Delta \mathbb{E}[f_{010}] \text{ [MHz] in } L^2$ $\Delta \mathbb{E}[f_{010}] \text{ [MHz] in } L^\infty$	805.08 8.053 10.818	794.633 8.068 11.28	1.298 ↓ 0.1865 ↑ 4.2322 ↑
Stroud-3 cubature, $K = 6$ $\mathbb{E}[f_{010}] \text{ (frequency) [MHz]}$ $\Delta \mathbb{E}[f_{010}] \text{ [MHz] in } L^2$ $\Delta \mathbb{E}[f_{010}] \text{ [MHz] in } L^\infty$	805.08 8.053 10.709	794.63 8.068 10.896	1.298 ↓ 0.1862 ↑ 1.7477 ↑
Stroud-2 cubature, $K = 4$ $\mathbb{E}[f_{010}]$ (frequency) [MHz] $\Delta \mathbb{E}[f_{010}]$ [MHz] in L^2 $\Delta \mathbb{E}[f_{010}]$ [MHz] in L^∞	805.08 8.053 10.876	794.63 8.068 10.982	1.298 ↓ 0.1866 ↑ 0.9771 ↑

^a $\Delta \mathbb{E}[f(\Omega^0)]$ in L^∞ is approximated using df and d²f for analytical solution. ^a $\Delta \mathbb{E}[f(\Omega^*)]$ in L^2 is approximated using df for first-order shape derivative.

sensitivity analysis has to be explored [21]

$$\operatorname{Var}\left[f_{i}\left(\mathbf{p}\right)\right] := \sum_{j=1}^{J} \left(\frac{\partial f_{i}\left(\mathbf{p}\right)}{\partial \overline{p}_{j}}\right)^{2} \sigma_{j}^{2}, \tag{45a}$$

with the normalized sensitivity coefficients given by

$$\eta^{i} = \frac{\operatorname{Var}\left[f_{i}\left(\mathbf{p}\right)\right]}{\sum_{i} \operatorname{Var}\left[f_{i}\left(\mathbf{p}\right)\right]} \in \left\langle 0, 1 \right\rangle. \tag{45b}$$

As in the case of variance-based sensitivity analysis (18), a large contribution to the frequency variance is if $\eta^i \approx 1$

Table 2. Means and P upper bounds in $\Omega^0(\overline{\mathbf{p}})$ and $\Omega^*(\overline{\mathbf{p}})$ pill-box model^{b.}

Quantity of interest	$F(\Omega^0)$	$F(\Omega^*)$	$\delta [\%]$
Analytical solution			
GH quadrature, $K = 27$ $\mathbb{E}[P(r)]$ (power loss) [W]	121.152	124.319	2.610↑
$\Delta \mathbb{E}[P(r)]$ [W] in L^2	2.4229	2.5245	4.1941 ↑
$\Delta \mathbb{E}[P(r)][W]$ in L^{∞}	3.7575	3.7612	0.8610 ↑
Stroud-5 cubature, $K = 14$			
$\mathbb{E}[P(r)]$ (power loss) [W]	121.152	124.319	2.610 ↑
$\Delta \mathbb{E}[P(r)]$ [W] in L^2	2.4229	2.5245	4.1941 ↑
$\Delta \mathbb{E}[P(r)] [W] \text{ in } L^{\infty}$	3.7428	3.7843	1.85 ↑
Stroud-3 cubature, $K = 6$			
$\mathbb{E}[P(r)]$ (power loss) [W]	121.152	124.319	2.610 ↑
$\Delta \mathbb{E}[P(r)]$ [W] in L^2	2.4229	2.5245	4.1934 ↑
$\Delta \mathbb{E}[P(r)] [W] \text{ in } L^{\infty}$	3.4287	3.4343	0.8590 ↑
Stroud-2 cubature, $K = 4$			
$\mathbb{E}[P(r)]$ (power loss) [W]	121.152	124.319	2.610 ↑
$\Delta \mathbb{E}[P(r)] [W] \text{ in } L^2$	2.4228	2.5243	4.1886 ↑
$\Delta \mathbb{E}[P(r)] [W] \text{ in } L^{\infty}$	3.3910	3.3843	0.4980 ↑
First-order shape derivative			
GH quadrature, $K = 27$			
$\mathbb{E}[P(r)]]$ (power loss) [W]	121.152	124.298	2.5962↑
$\Delta \mathbb{E}[P(r)]$ [W] in L^2	2.4229	2.5215	4.07 ↑
$\Delta \mathbb{E}[P(r)]] [W] \text{ in } L^{\infty}$	3.7575	3.7856	0.7489 ↑
Stroud-5 cubature, $K = 14$			
$\mathbb{E}[P(r)]$ (power loss) [W]	121.152	124.298	2.5962 ↑
$\Delta \mathbb{E}[P(r)]$ [W] in L^2	2.4229	2.5215	4.070 ↑
$\Delta \mathbb{E}[P(r)] [W] \text{ in } L^{\infty}$	3.7428	3.8030	1.6079 ↑
Stroud-3 cubature, $K = 6$			
$\mathbb{E}[P(r)]$ (power loss) [W]	121.152	124.298	2.5962 ↑
$\Delta \mathbb{E}[P(r)]$ [W] in L^2	2.4229	2.5215	4.069 ↑
$\Delta \mathbb{E}[P(r)]$ [W] in L^{∞}	3.4287	3.4544	0.7484 ↑
Stroud-2 cubature, $K = 4$			
$\mathbb{E}[P(r)]$ (power loss) [W]	121.152	124.298	2.5962 ↑
$\Delta \mathbb{E}[P(r)]$ [W] in L^2	2.4228	2.5213	4.065 ↑
$\Delta \mathbb{E}[P(r)] [W] \text{ in } L^{\infty}$	3.3910	3.4057	0.4327 ↑

^b $\Delta \mathbb{E}[P(\Omega^0)]$ in L^∞ is approximated using df and d²f for analytical solution. ^b $\Delta \mathbb{E}[P(\Omega^*)]$ in L^2 is approximated using df for first-order shape derivative.

holds. Otherwise, if $\eta^i \approx 0$, there exists only a small contribution, which is negligible. Typically, during the R_S measurements, the range of the peak magnetic field is assumed to be $B_0 = (10, \ldots, 120)$ [mT] with $\sigma_B = (0.096 \ldots, 0.11) \cdot B_0$ [mT] and the ambient pressure of $p_0 = 1.6$ [mbar] with $\sigma_p = 0.05 \cdot p_0$ [mbar], see, e.g. [8, 12]. Thus, depending on the scenario, the contribution of the static LF and air pressure to explaining the frequency variation when using (45a)–(45a) can vary between

$$\eta^{LF} = (0.03, 30.64, 87, 6) [\%], \ \eta^p = (99.97, 69.36, 12, 40) [\%]$$

for $B_0 = (10, 60, 120) [\text{mT}]$. Analogous results can be obtained for the simulation of the pressure fluctuations during the commissioning of the QPR. An exhaustive analysis of the static LF detuning for the QPR operation is given in [8]. Besides the static LF and microphonics, the dynamic LF detuning is also very prominent. In fact, under certain conditions of the dynamic LF or cavity deformation, mechanical oscillations can be triggered, which could lead to the simultaneous excitation of a dipole mode due to the breaking of the resonator's quadrupole symmetry [3, 6, 12]. Thus, to reflect the importance of both critical factors, especially the influence of dynamic LF detuning, in the steady-state stochastic coupled E-S-H model, we introduced:

- The scaling coefficient $\iota = \frac{\max_{x \in \Omega_R} |\mathbf{u}_{AP}|}{\max_{x \in \Omega_R} |\mathbf{u}_{AP}|} \approx 10$ for all the analyzed QPR's configurations, which permits statically to simulate the impact of both the ambient and (static/dynamic) LF radiation pressure into merit functions variations, which can mathematically be justified by the Cauchy–Schwarz inequality [82],
- The value of bent angles are assumed to be $\alpha = 0.15$ [deg], which corresponds to the deviation of the rods in x and y directions by [1mm], since the simulation of the breaking of the quadrupole symmetry allows for quantifying the observed measurement bias of the surface resistance for the third quadrupole mode [11, 18].

The deterministic material parameters used in the coupled simulations are summarized in table 4. Whereby, the Lamé coefficients of the materials can be calculated using

$$v = \frac{E}{2(1+\upsilon)}, \quad \eta = \frac{E\upsilon}{(1+\upsilon)(1-2\upsilon)}.$$

For the solution of the deterministic E-S-H problem, we have to simulate a full model of the QPR using tetrahedral finite elements within the range of 1 million for the MEVP and around 0.5 million in the case of the EVP and the HVP, respectively, using CST Studio Suite®. We used the built-in adaptive mesh refinement method to meet a tolerance of less than $\delta_n = 1 \cdot 10^{-6}$ in the computation of the quantities of interests.

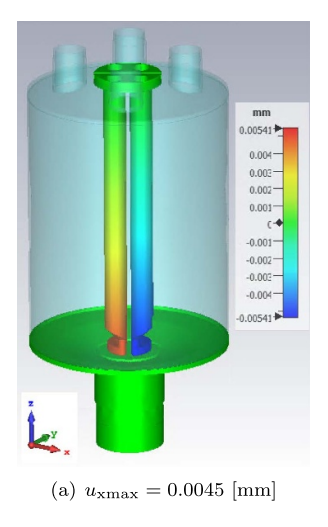
Furthermore, we have considered the homogenized PC expansion with the Hermite polynomial bases for the UQ studies since the geometrical variations are modeled by Gaussian distribution. Correspondingly, the magnitude of the perturbation δ_q regarding the production imperfections has been selected such that $\sigma_q = \delta_q \cdot \overline{p}_q[\text{mm}]$ for $q = 1 \dots, 8$. In the case of parameters related to the bent angles $p_{9/10}$, the variation has been assumed to be around 0.15 [deg]. For better readability, means and standard deviations of Gaussian design parameters are listed in table 3, while other deterministic material parameters used for solving the stochastic coupled E-S-H problem are summarized in table 4. The example results of the stress analysis of the HZB-QPR due to the static LF and the pressure of 1 bar when considering the mean geometrical and material parameters are depicted in figure 6 and 7, respectively. Specifically, the aforementioned figures illustrate the particular components of the displacement vector

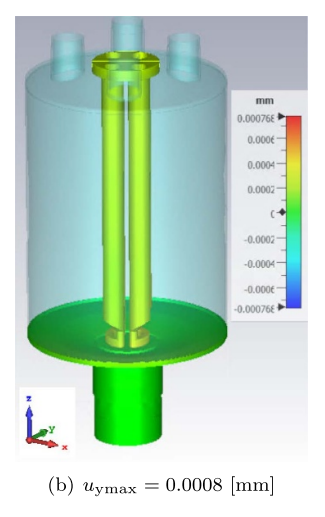
T-1-1- 0		1 4 1 1	· ·			ממו	C 4.
Table 3.	Means n.	and std. dev. σ	a of uncertain	geometric	parameters for ()PK C	configurations.

Parameter name		$\Omega_{\rm HZB}(\overline{\bf p})$ [3]	$\Omega_{\rm CERN}(\overline{\bf p})$ [19]	$\Omega_{Sol.A}(\overline{\mathbf{p}})$ [6]	$\Omega(\boldsymbol{\sigma})$ [3, 6]
p_1 (gap) (mm)		0.50	0.70	0.58	0.05
p_2 (rrods) (mm)		13.00	15.00	9.76	0.05
p_3 (hloop) (mm)		10.00	10.00	9.72	0.05
p_4 (rloop) (mm)		5.00	8.00	5.92	0.05
p_5 (wloop) (mm)		44.00	40.93	43.79	0.05
p_6 (dloop) (mm)		6.00	5.00	4.00	0.05
p ₇ (rcoil) (mm)		22.408	23.00	25.00	0.15
p_8 (rsample) (mm)		37.50	37.50	35.00	0.15
p_9 (angleBentRight)	(deg)	0.0	0.0	0.0	0.15
p_{10} (angleBentLeft)	(deg)	0.0	0.0	0.0	0.15

Table 4. Structural and thermal properties of materials used in simulations [83].

Material	Nb	Fe ₁₀₁₀	Cu
Density ρ (kg m ⁻³)	5700	7870	8930
Poisson's ratio $v[1/1]$	0.38	0.29	0.33
Young's modulus	62.1	205	120
E (GPa)			
Th. conduct.	0.1	65.2	401
$\kappa \mathrm{W} \mathrm{K}^{-1} m)$			
Specific heat	0.89	450	390
$C_{v} \mathrm{J}^{-1} \mathrm{K}^{-1} \mathrm{kg}^{-1}$			
Electr. conduct.	8.10^{13}	6.993	59.6
$\gamma~{ m MSm^{-1}}$			





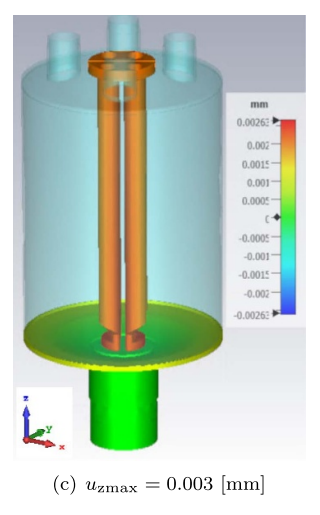


Figure 6. The components of the displacement \mathbf{u} due to static LF radiation pressure with max \mathbf{u} at the bottom of the pole shoes.

resulting from two distinct types of pressure, which were considered in the simulation. It is evident that the deformation of the rods and pole shoes due to the static LF radiation pressure is less pronounced than that resulting from the hydrostatic pressure. Nevertheless, as Slater's theorem indicates, even static detuning may result in a frequency shift, given the QPR's high susceptibility to mechanical perturbations. The aforementioned effect, in addition to the dynamic

LF and microphonics impact, can be observed in figure 4. Furthermore, the presented sensitivity analysis using (45a) serves to confirm this result. Moreover, as the sample temperature is dependent on a number of factors, including the applied RF field and the selected geometries and materials, the simulated temperature distribution due to power dissipation on stainless steel in the vicinity of the simplified flange is presented in figure 8. To conduct the UQ-based worst-case

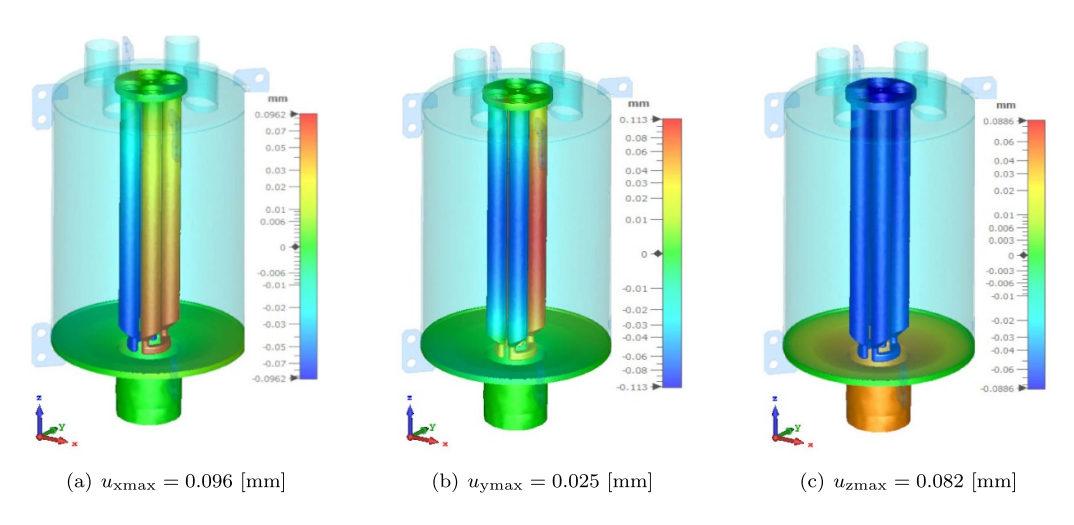


Figure 7. The components of the displacement **u** due to a vacuum pressure of 1 [bar] with max **u** at the bottom of the pole shoes.

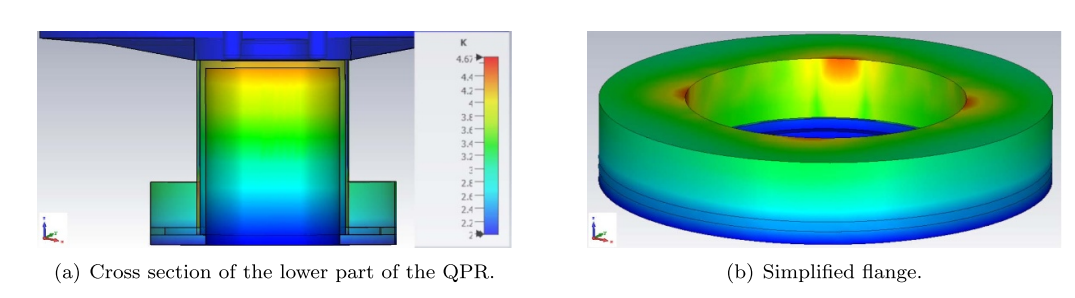


Figure 8. Simulated temperature distribution due to the power dissipation on the stainless steel flanges in the calorimetric chamber of the QPR.

expectation deformation analysis, we have used the procedure described in section 4, the flow of which has been described in pseudo-code and shown as Algorithm 1^{12} for clarity. The effect of atmospheric pressure and scaled LF radiation pressure by a factor of $\iota=10$, along with UQ analysis of the quadrupole symmetry breaking of the resonator, has been taken into account, resulting in the average maximal deformation in the range of max[$|(\mathbf{u}_{AP} + \iota \cdot \mathbf{u}_{LF})/2|$]. In essence, this approach is aligned with [11, 18] and allows us to reflect the impact of the LF detuning and hydrostatic pressure reported in [3, 8, 12].

The results of the deformation analysis with estimated performance objective variations due to the atmospheric and LF radiation pressure are summarized in Table 5. The configurations of the HZB-, CERN and Sol. A-types of QPR, optimized in [6], are analyzed in terms of design variations. Regarding the first three merit functions $F_1(\Omega^*)$, $F_2(\Omega^*)$, and $F_3(\Omega^*)$, which were of key importance to achieve an improved design of the QPR, we can conclude that shape variations have the least impact on the Sol. A configuration. It is particularly evident in the increased value of the dimensionless factor $F_3(\Omega^*)$, which quantifies the penetration of the magnetic field into the coaxial gap. This effect is also confirmed by the smallest temperature deviations (see $F_6(\Omega^*)$). As for the next two merit

Algorithm 1. UQ-based worst-case-expectation analysis.

```
1: Initialization:
        \Pi = (p_1, \ldots, p_Q), \, \boldsymbol{\rho}(\mathbf{p}), \, PCtype, PCorder, \, \mathbf{w}, \, \mathbf{p}^{(k)},
2:
3:
                         ⊳ (11), PCE param. & gener. weights & points
4: for k = 1..., K do
                                                           solve MVP(\mathbf{p}^{(k)}), (10a)
5:
                                                                \triangleright for eigenpairs E & f
           solve EVP(\mathbf{p}^{(k)}), (10b)
6:
                                                               \triangleright with (10d) for u & \sigma
           solve HVP(\mathbf{p}^{(k)}), (10c)
7:
                                                               \triangleright for T in deformed D
8: for i = \{1, ..., N\} do
                                                          9:
           \alpha_i \leftarrow \langle y_n(\mathbf{p}), \Phi_i(\mathbf{p}) \rangle

⊳ scalar product

10: for q = \{1, \dots, Q\} do
                                                 \tilde{y}_n \leftarrow \tilde{y}_n + \frac{\partial y_n}{\partial \overline{p}_q} \cdot S_{q,n} \cdot \max[|\mathbf{u}_q|]

    □ upper bound

12: Post-processing:
13: for i = \{1, ..., N\} do
                                                 \triangleright discrete projection loop for \tilde{y}_n
14:
              \tilde{\alpha}_i \leftarrow \langle \tilde{y}_n(\mathbf{p}), \Phi_i(\mathbf{p}) \rangle
                                                  \triangleright scalar product for updated \tilde{y}_n
           eval. \mathbb{E}\left[\tilde{y}_n\left(\mathbf{p}\right)\right], \operatorname{Var}\left[\tilde{y}_n\left(\mathbf{p}\right)\right]
                                                                 > statistical moments
16: for q = 1..., Q do
17:
                                                        ⊳ local & global sensitivity
```

functions $F_4(\Omega^*)$ and $F_5(\Omega^*)$, which are related to the ratio of the magnetic and electric peak values, the influence of shape variations caused by hydrostatic fluctuations and LF detuning is also the smallest. In addition, the performed estimation of merit function variations achieves the smallest uncertainty quantified by the mean worst-case upper bound error for the Sol. A configuration. Although the uncertainties in the mean

¹² In the case of the used Stroud-3 formula, the complexity of the developed algorithm is slightly improved by a factor of $2 \cdot (I-1)$ compared to the standard algorithm [23], and it equals K, where $K = 2 \cdot Q$ and I refers to the number of objective functions.

Table 5. Mean values and upper bounds of the merit functions calculated in case of the initial $\Omega^0(\bar{\mathbf{p}})$ and the deformed $\Omega^*(\bar{\mathbf{p}})$ QPR models.

Ouantities/									
Configurations	$\Omega_{ m HZB}^0(\overline{f p})$	$\Omega^*_{ m HZB}(\overline{f p})$	$^{\mathrm{a}}\delta[\%]$	$\Omega_{\mathrm{CERN}}^0(\overline{\mathbf{p}})$	$\Omega^*_{\mathrm{CERN}}(\overline{\mathbf{p}})$	$^{a}\delta[\%]$	$\Omega^0_{ m A}(ar{f p})$	$\Omega_{\rm A}^*(\overline{\bf p})$	$^{a}\delta[\%]$
$F_1(\Omega,\mathbf{h}) [\mathrm{M A}^2/\mathrm{J}]$	52.53	62.76	19.48 ↑	32.15	39.45	22.70 ↑	79.65	95.97	$20.49 \uparrow$
$^{\mathrm{b}}\Delta F_{1}(\Omega,\mathbf{h})~[\mathrm{MA^{2}/J}]$	6.849	5.985	$12.61 \downarrow$	4.917	3.079	37.37 ↓	12.23	6.975	$42.96 \downarrow$
$\delta F_1 = \Delta F_1/F_1$ [%]	13.04	9.54	×	15.29	7.80	×	15.35	7.27	×
$F_2(\Omega,\mathbf{h})$ [1/1]	0.122	0.114	786.9	0.177	0.162	3.06 ↔	0.180	0.172	4.83 ←
${}^{\mathrm{b}}\Delta F_{2}(\Omega,\mathbf{h})~[1/1]$	4.716μ	5.041μ	0.89 ♦	6.857μ	6.376μ	7.01	4.873μ	2.668μ	45.24 ↓
$^{c}\delta F_{2}=\Delta F_{2}/F_{2}~[\%]$	3.85	4.42	×	3.869	3.913	×	2.70	1.56	×
$F_3(\Omega,\mathbf{h}) [\mathrm{M}\ 1/1]$	0.126	0.087	30.47 ↓	0.175	0.134	23.03 \(\)	1.423	1.656	16.43 ↑
$^{\mathrm{b}}\Delta F_{3}(\Omega,\mathbf{h})~\mathrm{[M1/1]}$	1.06μ	0.25μ	76.74 ↓	0.048	0.027	44.42 ↓	0.512	0.294	42.58 ↓
$^{c}\delta F_{3}=\Delta F_{3}/F_{3}\left[\% ight]$	84.22	28.17	×	27.74	20.03	×	35.98	17.74	×
$F_4(\Omega,\mathbf{h})$ [1/1]	0.944	0.986	4.47 ↑	0.894	0.915	2.27 ↑	0.929	0.923	0.6 \(\)
${}^{\mathrm{b}}\Delta F_4(\Omega,\mathbf{h})~[1/1]$	42.14μ	25.32μ	$39.91 \downarrow$	0.014	0.008	$41.71 \downarrow$	21.29μ	4.55μ	78.62 ↓
$^{c}\delta F_{4}=\Delta F_{4}/F_{4}~[\%]$	4.46	2.56	×	1.52	98.0	×	2.29	0.49	×
$F_5(\Omega, \mathbf{h}) [\mathrm{mT}/(\mathrm{MV m}^{-1})]$	5.186	5.076	2.12 ↓	5.204	5.361	3.03 ↑	4.722	4.586	2.89 ↓
$^{\mathrm{b}}\Delta F_{5}(\Omega,\mathbf{h})\left[\mathrm{mT/(MVm^{-1})} ight]$	0.42	80.0	08.08	0.226	0.220	2.99 ↓	0.205	0.050	74.14 \downarrow
$^{c}\delta F_{5}=\Delta F_{5}/F_{5}~[\%]$	7.90	1.55	×	4.36	4.10	×	4.34	1.15	×
$F_6(\Omega,T)$ [K]	5.184	6.03	15.80 ↑	4.178	5.059	21.09 ↑	2.174	2.183	0.40 ↑
${}^{\mathrm{b}}\Delta F_{6}(\Omega,T)$ [K]	1.28	0.54	57.94 ↓	1.098	1.013	7.78	0.073	0.037	$49.63 \downarrow$
$^c\delta F_6=\Delta F_6/F_6~[\%]$	24.70	8.97	Х	26.29	20.02	X	3.37	1.69	X
$F_0(\Omega,\mathbf{h}) ext{ [GHz]}$	1.313	1.317	0.30 ↑	1.223	1.227	0.343 ↑	1.318	1.324	0.48
$^{\mathrm{b}}\Delta F_{0}(\Omega,\mathbf{h}) \; \mathrm{[MHz]}$	1.77	2.4	57.94 ↓	1.740	1.776	$2.20 \uparrow$	5.354	2.702	$49.53 \downarrow$
$^c\delta F_0=\Delta F_0/F_0~[\%]$	0.13	0.18	×	0.142	0.145	×	0.40	0.20	×

^a The columns denoted by δ with percentage [%] indicate a ratio (increase \uparrow /decrease \downarrow) of deformed configurations Ω_i^* to Ω_i^0 .

^b $\Delta F_i(\Omega^0)$] denotes an error bound in L^2 (standard deviation), calculated based on (16). $\Delta F_i(\Omega^*)$ denotes the mean worst-case upper bound error in L^∞ , computed using (22).

^c δF_i indicates the relative error in percentage.

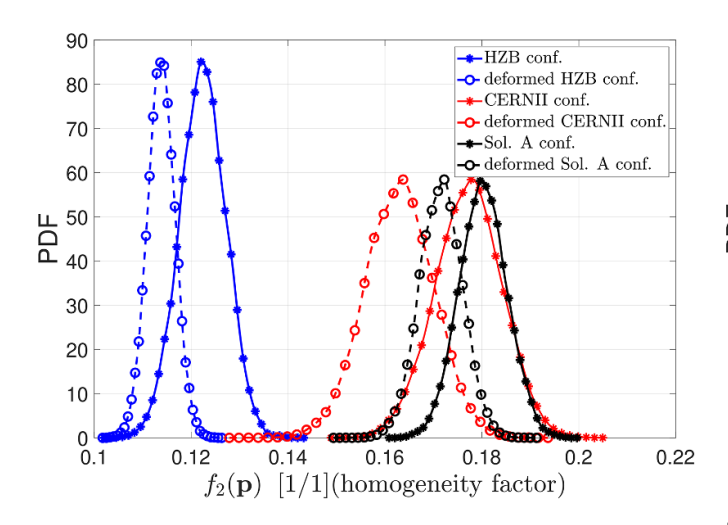


Figure 9. The frequency distribution in the studied QPR designs, including the deformation due to the scaled static LF.

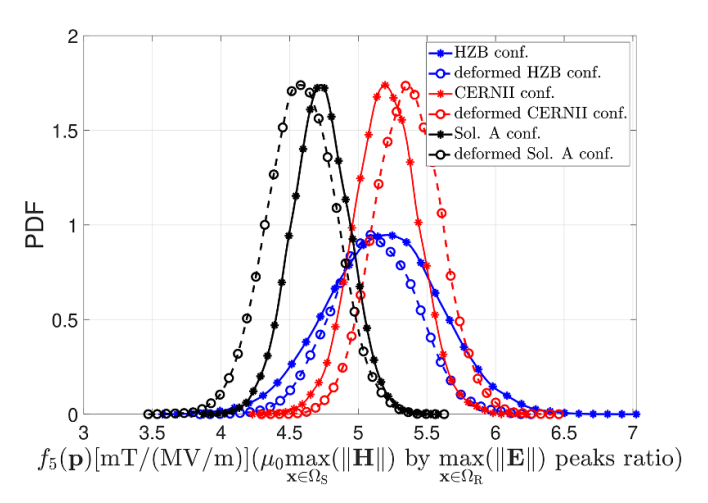


Figure 10. The maximum temperature distribution in the studied QPR designs, including the deformation due to the scaled static LF.

worst-case scenarios and the standard deviations cannot be directly compared, it can be observed that the former is about two times smaller than the ellipsoidal uncertainty set (standard deviations). Finally, the results of the worst-case deformation analysis can be compared qualitatively by examining the probabilistic density functions calculated before and after the design deformations, shown in figures 9–12, respectively.

6. Conclusion

To mitigate the influence of re-meshing errors in FEA on the estimation of merit function variations due to relatively small shape deviations, we have successfully developed an efficient tool to evaluate QPR designs under simulated harsh operating conditions. The developed coupled QPR model is a key of importance since the LF detuning might lead to the excitation of a dipole mode instead of a quadrupole mode [11]. Also, the hydrostatic fluctuation could have a significant impact on

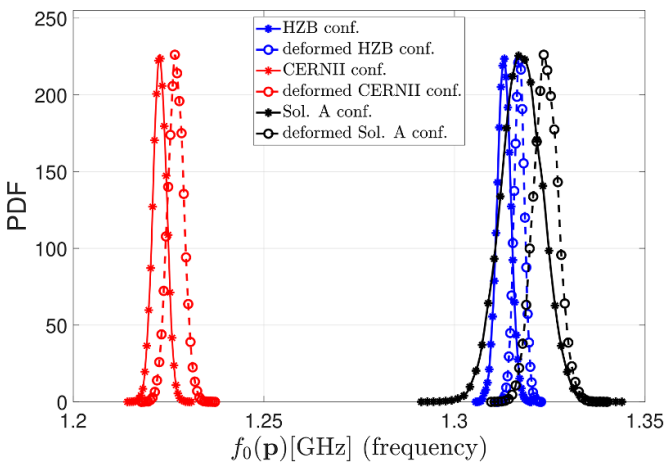


Figure 11. The distribution of the homogeneity factor in the studied QPR designs, including the deformation due to the scaled static LF.

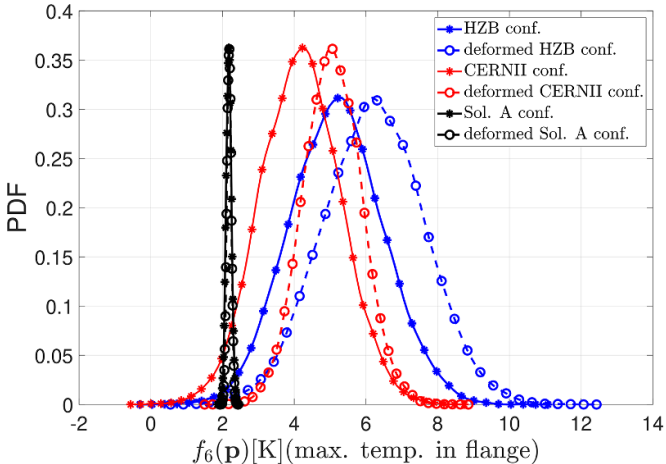


Figure 12. The distribution of the ratio of the maximum magnetic field vs. the maximum electric field in the studied QPR designs, including the deformation due to the scaled static LF.

the measurement procedures [8, 12]. The proposed procedure is based on the shape derivative framework combined with the UQ analysis. It enables finding not only the frequency shift due to the shape deviations as in the Slater formula [84], but also to employ user-defined merit function variations under geometric uncertainties, which broadens the CST Studio Suite® functionality in this respect.

The developed coupled E-S-H model is robust and yet adequately reflects the physical phenomena in a worst-case sense. On the one hand, it can be used to compare the existing QPR configurations to quantitatively explain the revealed biased surface resistance for the third operating mode. On the other hand, it is suitable for MO optimization since it takes into account the LF detuning and the influence of industrial imperfections. Its further application to design optimization under E-S-H coupling is considered to be the subject of the ongoing work.

The developed methodology can be successfully applied to the deformation analysis and optimization of various devices in accelerator physics, such as multi-cell cavities and couplers [1, 15, 23]. This includes consideration of different merit functions, such as those related to higher-order modes.

Data availability statement

All data that support the findings of this study are included within the article (and any supplementary files).

Acknowledgments

This work has been supported by the German Federal Ministry for Research and Education BMBF under contract 05H21HRRB1. Furthermore, the authors would like to thank Dr S Gorgi Zadeh (CERN Switzerland) for his help in the efficient modeling and simulations of the QPR structures.

Appendix. Shape derivatives

This section details the derivation of the shape sensitivity for the stochastic MEVP of (10a). We distinguish between self-adjoint operators like eigenfrequency, $\lambda = 1.3$ [GHz], and others, which result in formulae (36a) and (38), respectively. In both cases, the starting points are the Lagrangians defined by (34) and (35), similar to optimal control problems constrained by stochastic PDE's [45, 85].

Typically, finding the shape derivative for a nonlinear PDE requires the analysis of the convergence of $w^{\tau} = (u^{\tau} - u)/\tau$ to the material derivative \dot{w} of (27) in the weak or the strong sense [60, 65, 66]. However, for a problem described by (34) and (35) with constant material coefficients ϵ and μ , following the procedure proposed in [58], we can directly use (28) and (30) to find the stationarity of the Lagrangians, thus providing the optimality conditions.

Due to physics principles, the eigenpair of the third operational QPR mode is assumed to be simple and therefore shape-differentiable [58, 61]. Next, suppose the material derivative and the expectation operator commute with each other under some regularity assumptions [71]. Then, by applying the material derivative from (28) and using the commutative property of partial derivatives with respect to τ and x for $\mathcal{L}_0(\mathbf{h}_{\tau}, \lambda_{\tau}, \boldsymbol{\varphi}_{\tau}, \zeta_{\tau})$ yields its variation with respect to the design

$$\begin{split} \left[\mathcal{L}_{0}\left(\cdot\right)\right]' &= +\mathbb{E}\left[\left\langle \epsilon_{r}^{-1}\nabla\times\mathbf{h},\nabla\times\boldsymbol{\varphi}'\right\rangle_{\Omega}\right] \\ &+ \mathbb{E}\left[\left\langle \epsilon^{-1}\nabla\times\mathbf{h}',\nabla\times\boldsymbol{\varphi}\right\rangle_{\Omega}\right] \\ &+ \mathbb{E}\left[\lambda\left\langle\mu_{r}\mathbf{h},\boldsymbol{\varphi}'\right\rangle_{\Omega}\right] \\ &- \mathbb{E}\left[\lambda\left\langle\mu_{r}\mathbf{h}',\boldsymbol{\varphi}\right\rangle_{\Omega}\right] - \mathbb{E}\left[\zeta\left\langle\mu_{r}\mathbf{h},\mathbf{h}'\right\rangle_{\Omega}\right] \\ &+ \mathbb{E}\left[\left\langle\epsilon_{r}^{-1}\mathbf{n}\times\mathbf{h},\mathbf{n}\times\boldsymbol{\varphi}'\right\rangle_{\gamma}\right] \end{split}$$

$$+ \mathbb{E}\left[\left\langle \epsilon_{r}^{-1} \boldsymbol{n} \times \boldsymbol{h}', \boldsymbol{n} \times \boldsymbol{\varphi} \right\rangle_{\gamma}\right]$$

$$+ \mathbb{E}\left[\left\langle \epsilon_{r}^{-1} \nabla \times \boldsymbol{h}, \nabla \times \boldsymbol{h} \right\rangle_{\partial \Omega}\right] - \mathbb{E}\left[\lambda \left\langle \mu_{r} \boldsymbol{h}, \boldsymbol{\varphi} \right\rangle_{\partial \Omega}\right]$$

$$+ \mathbb{E}\left[\zeta \left\langle \mu_{r} \boldsymbol{h}, \boldsymbol{h} \right\rangle_{\partial \Omega}\right]$$

$$+ \mathbb{E}\left[\left\langle \epsilon_{r}^{-1} \boldsymbol{n} \times \boldsymbol{h}, (\boldsymbol{n} \times \boldsymbol{\varphi}) \kappa v_{n} \right\rangle_{\gamma}\right]$$

$$- \mathbb{E}\left[f_{0}'\right] + \mathbb{E}\left[\lambda' \left\langle \mu_{r} \boldsymbol{h}, \boldsymbol{\varphi} \right\rangle_{\Omega}\right], \tag{A.1}$$

where the null terms related to partial derivatives of the coefficients have already been omitted and $f_0' = 1$, $\lambda' = 1$, $\varphi' \equiv \dot{\varphi} - \nabla \varphi$, $\mathbf{h}' \equiv \dot{\mathbf{h}} - \nabla \mathbf{h}$. In fact, since $\dot{\varphi} \in V_\rho$ the integral terms involving it in (A.1) vanish [58]. Furthermore, setting $[\mathcal{L}_0(\cdot)]' = 0$ and collecting all the integral terms related to $\dot{\mathbf{h}}$ allows to deduct the adjoint eigenvalue problem

$$\nabla \times \left(\epsilon_r^{-1} \nabla \times \boldsymbol{\varphi}\right) - \lambda \mu_r \boldsymbol{\varphi} + \mu_r \zeta \mathbf{h} = 0 \quad \text{in } D \text{ a.e. } \mathbf{p} \in \Gamma,$$

$$\boldsymbol{n} \times \boldsymbol{\varphi} = 0 \quad \text{on } \partial D \text{ a.e. } \mathbf{p} \in \Gamma,$$

$$\boldsymbol{n} \times \epsilon_r^{-1} \nabla \boldsymbol{\varphi} = 0 \quad \text{on } \partial D \text{ a.e. } \mathbf{p} \in \Gamma,$$

$$\mathbb{E} \left[\langle \mu_r \boldsymbol{\varphi} . \mathbf{h} \rangle_{\mathcal{O}} \right] = -\mathbb{E} \left[f_0' \right], \tag{A.2}$$

where a.e is the abbreviation for almost everywhere. Here, for better readability the dependence of eigenpair $\{\mathbf{h}(\mathbf{x},\mathbf{p}),\lambda(\mathbf{p})\}=\{\mathbf{h},\lambda\}$ and adjoint eigenpair $\{\varphi(\mathbf{x},\mathbf{p}),\lambda(\mathbf{p})\}=\{\varphi,\lambda\}$ have been suppressed. Finally, this special structure of the adjoint problem allows us to rewrite the solution to the shape derivative directly in the form of (36a) by proving $\varphi=-\mathbf{h}$, as shown in [58, 69], and then using the normalization condition and the formula (32)–(33).

The optimality system related to $\mathcal{L}_2(\mathbf{h}_{\tau}, \lambda_{\tau}, \varphi_{\tau}, \zeta_{\tau})$ can be derived in the same fashion as for \mathcal{L}_0 . Here, it is assumed that $f_1(\mathbf{h}), \nabla \times \mathbf{h}) \Big|_{\partial \Omega}$ is a scalar well-defined, finite valued, continuous, convex and differentiable function with respect to \mathbf{h} and $\nabla \times \mathbf{h}$. Moreover, since the material derivative is the directional derivative, the subdifferential and expectation operators can be interchanged [29]. Thus, taking the material derivative of \mathcal{L}_2 with respect to the design leads to the variation

$$\begin{split} \left[\mathcal{L}_{2}(\cdot) \right]' &= + \mathbb{E} \left[\left\langle \boldsymbol{\epsilon}_{r}^{-1} \nabla \times \mathbf{h}, \nabla \times \boldsymbol{\varphi}' \right\rangle_{\Omega} \right] \\ &+ \mathbb{E} \left[\left\langle \boldsymbol{\epsilon}^{-1} \nabla \times \mathbf{h}', \nabla \times \boldsymbol{\varphi} \right\rangle_{\Omega} \right] \\ &+ \mathbb{E} \left[\lambda \left\langle \boldsymbol{\mu}_{r} \mathbf{h}, \boldsymbol{\varphi}' \right\rangle_{\Omega} \right] \\ &- \mathbb{E} \left[\lambda \left\langle \boldsymbol{\mu}_{r} \mathbf{h}', \boldsymbol{\varphi} \right\rangle_{\Omega} \right] - \mathbb{E} \left[\zeta \left\langle \boldsymbol{\mu}_{r} \mathbf{h}, \mathbf{h}' \right\rangle_{\Omega} \right] \\ &+ \mathbb{E} \left[\left\langle \boldsymbol{\epsilon}_{r}^{-1} \mathbf{n} \times \mathbf{h}, \mathbf{n} \times \boldsymbol{\varphi}' \right\rangle_{\gamma} \right] + \mathbb{E} \left[\left\langle \boldsymbol{\epsilon}_{r}^{-1} \mathbf{n} \times \mathbf{h}', \mathbf{n} \times \boldsymbol{\varphi} \right\rangle_{\gamma} \right] \\ &+ \mathbb{E} \left[\left\langle \boldsymbol{\epsilon}_{r}^{-1} \nabla \times \mathbf{h}, \nabla \times \boldsymbol{h} \right\rangle_{\partial \Omega} \right] - \mathbb{E} \left[\lambda \left\langle \boldsymbol{\mu}_{r} \mathbf{h}, \boldsymbol{\varphi} \right\rangle_{\partial \Omega} \right] \\ &+ \mathbb{E} \left[\zeta \left\langle \boldsymbol{\mu}_{r} \mathbf{h}, \mathbf{h} \right\rangle_{\partial \Omega} \right] + \mathbb{E} \left[\left\langle \boldsymbol{\epsilon}_{r}^{-1} \mathbf{n} \times \mathbf{h}, (\mathbf{n} \times \boldsymbol{\varphi}) \kappa \boldsymbol{v}_{n} \right\rangle_{\gamma} \right] \\ &- \left\langle \chi_{1} D_{\mathbf{h}} f_{1}, \mathbf{h}' \right\rangle_{\gamma} - \left\langle \chi_{1} f_{1}, f_{1} \kappa \mathbf{v} \cdot \boldsymbol{n} \right\rangle_{\gamma} \\ &- \left\langle \chi_{1} D_{\nabla \times \mathbf{h}} f_{1}, \nabla \times \mathbf{h}' \right\rangle_{\gamma} + \mathbb{E} \left[\lambda' \left\langle \boldsymbol{\mu}_{r} \mathbf{h}, \boldsymbol{\varphi} \right\rangle_{\Omega} \right], \end{split} \tag{A.3}$$

where $D_{\mathbf{h}}f_1 \equiv \partial f_1/\partial \mathbf{h}$, $\lambda' = 1$ and $D_{\nabla \times \mathbf{h}}f_1 \equiv \partial f_1/\partial (\nabla \times \mathbf{h})$, and $\varphi' \equiv \dot{\varphi} - \nabla \varphi$, $\mathbf{h}' \equiv \dot{\mathbf{h}} - \nabla \mathbf{h}$. Then, the weak form of the adjoint system formulated by selecting the integral terms with $\dot{\mathbf{h}}$ is defined by (37) with the orthogonality condition between φ and \mathbf{u} given by (37b). Ultimately, the shape derivative of f_2 functionals of (20b)–(20g) is expressed by (38).

Alternatively, one can apply the methodology proposed by [61] in deterministic settings, which leads to the same results for the frequency shift estimation.

ORCID iDs

Piotr Putek https://orcid.org/0000-0002-7350-7510 Simon B Adrian https://orcid.org/0000-0001-8008-6235 Marc Wenskat https://orcid.org/0000-0001-6546-770X Ursula van Rienen https://orcid.org/0000-0003-1042-2058

References

- [1] Padamsee H, Knobloch J and Hays T 2008 RF Superconductivity for Accelerators (Wiley)
- [2] Junginger T 2012 Investigation of the surface resistance of superconducting materials *PhD Thesis* University of Heidelberg
- [3] Kleindienst R 2017 Radio frequency characterization of superconductors for particle accelerators *PhD Thesis* University of Siegen
- [4] Knobloch J *et al* 1999 High-field q slope in superconducting cavities due to magnetic field enhancement at grain boundaries *Proc. 9th Workshop on RF Superconductivity* (Citeseer) pp 77–91
- [5] Bellandi A 2021 LLRF control techniques for the european xfel continuous wave upgrade *PhD Thesis* Staats-und Universitätsbibliothek Hamburg Carl von Ossietzky
- [6] Putek P, Zadeh S G, Wenskat M and van Rienen U 2022 Phys. Rev. Accel. Beams. 25 012002
- [7] Mahner E, Calatroni S, Chiaveri E, Haebel E and Tessier J 2003 Rev. Sci. Instrum. 74 3390–4
- [8] Monroy Villa R 2023 Development of a test resonator for investigations of the RF properties of superconducting materials *PhD Thesis* Universität Hamburg
- [9] Monroy-Villa R, Zadeh S G, Hillert W, Lemke M, Putek P, Reschke D, Röhling M, Thie J and Wenskat M 2022 Status of the New Quadrupole Resonator for SRF R&D *Proc.* SRF'21Int. Conf. on RF Superconductivity (Geneva, Switzerland) (JACoW Publishing) pp 751–5
- [10] Aull S, Doebert S, Junginger T and Knobloch J 2013 High resolution surface resistance studies *Proc. SRF'13 Int. Conf.* on RF Superconductivity (Geneva, Switzerland) (JACoW Publishing) pp 785–8
- [11] Keckert S, Junginger T, Knobloch J and Kugeler O 2018 The challenge to measure nΩ Surface Resistance on SRF Samples (Proc. 9th Int. Particle Accelerator Conf. (IPAC'18)) pp 2812–5
- [12] Keckert S 2019 Characterization of Nb3Sn and multilayer thin films for SRF applications *PhD thesis* Universität Siegen
- [13] Keckert S et al 2021 AIP Adv. 11 125326
- [14] Munoz J, Bermejo F, De Estructura I and Materia D 2013

 Lorentz force detuning simulations of spoke cavities with different stiffening elements *Proc. SRF'13 Int. Conf. on RF Superconductivity (Geneva, Switzerland JACoW Publishing*) pp 946–9
- [15] Schreiber U and van Rienen U 2006 Coupled Calculation of Electromagnetic Fields and Mechanical Deformation Scientific Computing in Electrical Engineering (Springer) pp 63–68
- [16] Keckert S, Kleindienst R, Kugeler O, Tikhonov D and Knobloch J 2021 Rev. Sci. Instrum. 92 064710

- [17] Brackebusch K and van Rienen U 2015 *IEEE Trans. Magn.* 52 1–4
- [18] Putek P, Zadeh S G, Wenskat M, Hillert W and van Rienen U 2019 Uncertainty quantification of a quadrupole-resonator for radio frequency characterization of superconductors *Proceedings-the 19th Int. Conf. RF Superconductivity* (SRF19) (Dresden, Germany) pp 1170–4
- [19] del Pozo Romano V, Gerigk F, Betemps R, Illan Fiastre R and Mikkola T 2017 Redesign of CERN's quadrupole resonator for testing of superconducting samples 18th Int. Conf. on RF Superconductivity, SRF2017 (Lanzhou, China) pp 420–2
- [20] Augustin F, Gilg A, Paffrath M, Rentrop P and Wever U 2008 Eur. J. Appl. Math. 19 149–90
- [21] Yao W, Chen X, Luo W, van Tooren M and Guo J 2011 Prog. Aerosp. Sci. 47 450–79
- [22] Kugelmann B and Pulch R 2018 IFAC-papersonline 9th Vienna Int. Conf. on Mathematical Modelling vol 51 pp 7–12
- [23] Putek P, Zadeh S G and van Rienen U 2024 J. Comput. Phys. 513 113125
- [24] Harbrecht H 2010 Math. Methods Appl. Sci. 33 91–102
- [25] Andrietti S, Chenot J L, Bernacki M, Bouchard P O, Fourment L, Hachem M and Perchat E 2015 Comput. Methods Mater. Sci. 15 265–93
- [26] Reitzinger S, Wabro M and Zaglmayr S 2012 Sensitivity Analysis for Maxwell Eigenvalue Problems in Industrial Applications (Advanced Finite Element Methods and Applications) (Springer) pp 239–56
- [27] Babuška I and Chleboun J 2002 Math. Comput. 71 1339-70
- [28] Babuška I, Nobile F and Tempone R 2005 *Numer. Math.* **101** 185–219
- [29] Shapiro A, Tekaya W, Soares M P and da Costa J P 2013 Oper. Res. 61 1435–49
- [30] Lamberti P D and Zaccaron M 2021 Math. Methods Appl. Sci. 44 10477–500
- [31] Herter C, Schöps S and Wollner W 2023 Proc. Appl. Math. Mech. 22 e202200122
- [32] Wieners C and Xin J 2013 *Math. Methods Appl. Sci.* **36** 2524–39
- [33] Weiland T 1984 Part. Accel. 17 227-42
- [34] Babuška I and Osborn J E 1989 *Math. Comput.* **52** 275–97
- [35] Arbenz P, Geus R and Adam S 2001 Phys. Rev. Spec. Top.-Accel. 4 022001
- [36] Boffi D, Brezzi F and Gastaldi L 1997 Ann. Sc. Norm. Super. Pisa - Cl. Sci. 25 131–54
- [37] Hiptmair R 2002 Acta Numer. 11 237-339
- [38] Brenner S C 2008 The Mathematical Theory of Finite Element Methods (Springer)
- [39] Babuška I and Strouboulis T 2001 *The Finite Element Method* and its Reliability (Oxford University Press)
- [40] Wiener N 1938 Am. J. Math. 60 897-936
- [41] Cameron R H and Martin W T 1947 Ann. Math. 48 385–92
- [42] Xiu D and Karniadakis G E 2002 Comput. Methods Appl. Mech. Eng. 191 4927–48
- [43] Malliavin P 2006 Stochastic Calculus of Variations in Mathematical Finance (Springer)
- [44] Babuska I, Tempone R and Zouraris G E 2004 SIAM J. Numer. Anal. 42 800–25
- [45] Tiesler H, Kirby R M, Xiu D and Preusser T 2012 SIAM J. Control Optim. 50 2659–82
- [46] Xiu D 2007 Commun. Comput. Phys. 2 293-309
- [47] Xiu D and Karniadakis G E 2002 *SIAM J. Sci. Comput.* **24** 619–44
- [48] Ghanem R G and Spanos P D 2003 Stochastic Finite Elements: a Spectral Approach (Springer)
- [49] Le Mitre O and Knio O M 2010 Spectral Methods for Uncertainty Quantification: With Applications to Computational Fluid Dynamics (Springer)

- [50] Xiu D 2010 Numerical Methods for Stochastic Computations: A Spectral Method Approach (Princeton University Press)
- [51] Matthies H G and Keese A 2005 Comput. Methods Appl. Mech. Eng. 194 1295–331
- [52] Xiu D 2009 Commun. Comput. Phys. 5 242-72
- [53] Sobol I M 1993 Math. Modeling Comput. Exp. 1 407–13
- [54] Sudret B 2008 Reliab. Eng. Syst. Safe. 93 964-79
- [55] Babuška I, Nobile F and Tempone R 2010 SIAM Rev. 52 317–55
- [56] Bagci H, Yucel A C, Hesthaven J S and Michielssen E 2009 IEEE Trans. Electromagn. Compat. 51 301–11
- [57] Benner P and Schneider J 2015 Int. J. Uncertain. Quan. 5 195–208
- [58] Komkov V 1984 Sensitivity of Functionals With Applications to Engineering Sciences (Springer)
- [59] Sokolowski J and Zolesio J P 1992 Introduction to Shape Optimization: Shape Sensitivity Analysis (Springer)
- [60] Ito K, Kunisch K and Li Z 2001 *Inverse Problems*
- [61] Allaire G and Jouve F 2005 Comput. Methods Appl. Mech. Eng. 194 3269–90
- [62] Babuška I and Chleboun J 2003 Numer. Math. 93 583-610
- [63] Bucur D and Zolésio J-P. 1997 Ann. Math. Pura Appl. 173 127–43
- [64] Hiptmair R and Li J 2013 Ann. Math. Pura Appl. **192** 1077–98
- [65] Cimrák I 2012 SIAM J. Numer. Anal. 50 1086-110
- [66] Putek P 2019 Eng. Opt. 51 2169-92
- [67] Mores W, Nimmegeers P, Hashem I, Bhonsale S S and Van Impe Jan F.M. 2023 Comput. Chem. Eng. 169 108099
- [68] Chen S and Chen W 2011 Struct. Multidiscipl. Optim. 44 1–18
- [69] Akçelik V, Biros G, Ghattas O, Keyes D, Ko K, Lee L Q and Ng E G 2005 Adjoint methods for electromagnetic shape

- optimization of the low-loss cavity for the international linear collider *J. Phys.: Conf. Ser.* **16** 435–45
- [70] Gunzburger M D 2002 Perspectives in Flow Control and Optimization (SIAM)
- [71] Gatarek D and Sokołowski J 1992 Shape Sensitivity Analysis for Stochastic Evolution Equations (Boundary Control and Boundary Variation) J P Zoléesio (Springer) pp 215–20
- [72] Çiloğlu P and Yucel H 2023 Adv. Comput. Math. 49 16
- [73] Choi K K 1987 Shape Design Sensitivity Analysis and Optimal Design of Structural Systems (Springer)
- [74] Yang R and Botkin M 1987 AIAA J. 25 492-7
- [75] Zhang S and Belegundu A 1992 Struct. Multidisci. Opt. 5 84–94
- [76] Li D, Corlett J and Turner W 1998 Temperature Distribution Calculations on Beryllium Windows in RF Cavities for a Muon Collider Proc. LINAC'98 (Linear Accelerator Conference) (Chicago, IL, USA, August 1998) vol 10 pp 273–5 (available at: https://jacow.org/198/papers/MO4089. pdf)
- [77] Timoshenko S and Goodier J 1970 New York
- [78] Pozar D M 2011 Microwave Engineering (Wiley)
- [79] Parise M 2018 J. Instrum. 13 T05010
- [80] Slaughter W S 2012 The Linearized Theory of Elasticity (Springer)
- [81] Xiu D 2008 Appl. Numer. Math. 58 1515-20
- [82] Solín P 2005 Partial Differential Equations and the Finite Element Method (Wiley)
- [83] Collings E 2013 Applied Superconductivity, Metallurgy and Physics of Titanium Alloys: Fundamentals Alloy Superconductors: Their Metallurgical, Physical and Magnetic-Mixed-State Properties (Springer)
- [84] Slater J C 1946 Rev. Mod. Phys. 18 441
- [85] Rosseel E and Wells G N 2012 Comput. Methods Appl. Mech. Eng. 213 152–67